

Radiation-dominated polar emitting region of an accreting X-ray pulsar – I. Polarization- and spectrum-dependent structure, and the emergent continuum

M. I. Gornostaev^{*}

Sternberg Astronomical Institute, Lomonosov Moscow State University, Universitetskij pr. 13, Moscow 119234, Russia
Faculty of Physics, Lomonosov Moscow State University, Leninskie Gory 1-2, Moscow 119991, Russia

Accepted XXX. Received YYY; in original form ZZZ

ABSTRACT

The radiation-dominated polar emitting region of an accreting X-ray pulsar is simulated numerically in the framework of a three-dimensional (geometrically two-dimensional) model. The radiative transfer within the emitting region and the structure of the latter are calculated with the use of the self-consistent algorithm developed earlier. The magnetic scattering cross sections dependent on the photon energy and polarization have been incorporated. Second-order bulk Comptonization over entire emitting region, induced Compton scattering, the switching of the polarization modes, free-free processes, the cyclotron emission because of electron-proton collisions, and a realistic shape of the accretion channel have been taken into account. The case of a dipole magnetic field is considered. It is shown that the induced Compton effect can play a notable role in establishing the electron temperature in the post-shock zone. Within the model shock wave, a higher electron temperature is achieved than in the post-shock zone by means of the bulk-heating mechanism. The photons gaining the energy in the shock wave and above it due to bulk motion effects and the thermal Doppler effect are responsible for the formation of high-energy regions in the emergent continuum of the polarization modes.

Key words: radiative transfer – radiation: dynamics – shock waves – stars: neutron – pulsars: general – X-rays: binaries

1 INTRODUCTION

An accreting X-ray pulsar (Giacconi et al. 1971) is included in a binary system, magnetized neutron star on to which a plasma inflows from a companion star (e.g. Pringle & Rees 1972; Davidson & Ostriker 1973; Baan & Treves 1973). The accreting material is directed towards the neutron star along the magnetic field lines, increasing the kinetic energy, the main fraction of which is eventually released as the energy of X-ray photons emerging from heated to corresponding temperatures regions of the atmosphere of the neutron star or those grown above the star. Usually, the areas of the emitting regions across the magnetic field are much smaller than the area of the neutron star surface, and the magnetic and rotational axes of the neutron star are far enough apart to coincide. Hence, the rotation of the neutron star provides the possibility of the formation of the pulses

of the X-ray radiation that comes from those regions to a distant observer.

When the mass accretion rate is sufficient, above the neutron star surface, inside the accretion channel, the region containing the slowed plasma flow appears having, on average, a notably larger transverse Thomson optical depth than the freely falling flow. Such structures are often referred to as the accretion columns. Under certain circumstances, the radiation pressure in the structure is much greater than the gas pressure. Photons diffused from the almost stagnate interiors are then advected by the compressed heated flow to the neutron star surface (diffusing at the same time across the magnetic field), to a region near the side boundary of the channel, so that such a structure turns out to be surrounded by a radiation-dominated shock wave (Davidson & Ostriker 1973; Davidson 1973; de Hoffmann & Teller 1950; Marshak 1958).

It is well known that modelling the deceleration of the accretion flow in a radiation-dominated shock wave is an example of a problem, that has not yet been consid-

^{*} E-mail: mgornost@gmail.com

ered exhaustively in the framework of a unitary study. The 2D numerical solution of Davidson (1973) became the first quantitative theoretical result showed the structure of the emitting region formed in sufficiently luminous accretion-powered X-ray pulsars. A one-dimensional approximation of the initially 2D equations from this work was considered by Basko & Sunyaev (1976). Blandford & Payne (1981a) derived in the Fokker-Planck approximation the radiative transfer equation (Chandrasekhar 1960; Mihalas 1978) for the compressed flow of a plasma. This result is used in most of the papers on the spectral radiative transfer in the accretion columns listed in the next two paragraphs. In the papers by Blandford & Payne (1981b) and Lyubarskii & Syunyaev (1982), the solutions for the spectrum of radiation of a 1D radiation-dominated shock were studied.

Wang & Frank (1981) obtained a number of 2D numerical solutions for the steady-state structure of the column. Kirk (1985) developed a 2D analytical solution for the structure of the radiation-dominated column at luminosities at which the optically thick zone of the column has a relatively small height. Arons, Klein & Lea (1987) described the processes taking place in a strongly magnetized plasma under the conditions of accretion columns. The first computational steps to solve the problem in a self-consistent way were carried out in the following three works. Riffert (1988) considered in the grey approximation a self-consistent 1D problem of the dynamics, electron temperature and radiative transfer inside the column. Rebetzky et al. (1988) modelled the 2D column structure and solved the 3D (geometrically 2D) radiative transfer equation for the mode-summed spectral intensity in an uncoupled manner, and the frequency-dependent diffusion coefficients were used. Rebetzky et al. (1989) obtained a 3D self-consistent solution describing the 2D structure of the column and the total emergent spectrum, and the frequency-integrated energy equation was included in the computational procedure. Thermal Comptonization was neglected and bulk motion effects of second order in the velocity were not taken into account. Only cases of relatively low accretion rates were considered, at which the radiation pressure effects become dynamically significant, so that typical obtained absolute values of the divergence of the bulk velocity turned out to be relatively small. The angular distributions of the intensity of radiation emergent from the sidewall of the accretion channel were obtained with the use of the method of last scattering by Kraus et al. (1989). Maile et al. (1989) studied the effects of the bulk motion on the radiation patterns from the side boundary of the flow formed at different frequencies solving a simplified coherent radiation transfer equation under the conditions of the moving material.

Burnard, Arons & Klein (1991) calculated the spectra of the normal polarization modes from a preset radiation-dominated mound with taking into account the angular photon redistribution using the Feautrier method (Burnard, Klein & Arons 1988, 1990), and the processes in the shock wave and above were neglected. The inclusion of the photon bubble oscillations in the numerical calculations of the radiation-dominated accretion column was performed by Klein & Arons (1989) (see also Arons 1992; Klein et al. 1996; Hsu, Arons & Klein 1997). A steady-state 1D dynamical model of the cylindrical column was developed by Becker (1998). Analytical solutions for the radiative transfer equa-

tion represented in the Fokker-Planck approximation for such a column were obtained by Becker & Wolff (2005, 2007) with making use of the velocity profiles allowing the separation of variables, but different from linear ones. Numerical solution of the spatially 1D radiative transfer equation with the use of the phenomenological power-law velocity profiles was carried out by Farinelli et al. (2012, 2016). Mushtukov et al. (2015a) obtained an expression for the critical luminosity and some solutions describing the structure of the column. West, Wolfram & Becker (2017a,b) self-consistently simulated the column taking into consideration the equations of state for the two-component plasma. The structure of the flow was supposed to be one-dimensional. Gornostaev (2021) (hereafter referred to as G2021) solved numerically the problems of the 3D dynamical structure of the inclined accretion columns, and (in a self-consistent way) the geometrically 2D problem of the structure of the column and its emergent spectrum, regardless of the straightforward observational applications (the gas pressure was neglected). The MHD simulations of the 2D structure of the column were performed by Zhang, Blaas & Jiang (2021, 2022), and development of the photon bubble instability was confirmed. Becker & Wolff (2022) took into account the upward widening of the accretion channel, analysed different velocity profiles (including those for the gas-dominated column), and added to their previous considerations some calculations of the cross sections in a strong magnetic field.

The structure of the accretion column should be interpreted as primarily dynamical one in the description above. There are not many attempts not based on thermalization-related predictions using the Stefan-Boltzmann law to calculate the thermal properties of the column. Although establishing the temperature of electrons inside the radiation-dominated plasma in accordance with the local Compton equilibrium was mentioned repeatedly (e.g. Blandford & Payne 1981a; Lyubarskii & Syunyaev 1982; Becker & Wolff 2007; Zel'dovich & Levich 1970; Illarionov & Syunyaev 1975b), the use of the specified approximation in calculations of the structure of the accretion column is quite rare (Riffert 1988; West et al. 2017a,b; G2021). Often the temperature was set constant and parametrized (e.g. Becker & Wolff 2007, 2022).

It seems that a physically consistent modelling of the radiative transfer and accretion column structure taking into consideration the entire diversity of non-stationary processes, inhomogeneities in the gas flow, the influence of the gas component, and including the calculation of cyclotron processes and polarization of the radiation is a multidimensional problem which still does not have complete solution (Arons et al. 1987). Many years have passed since the estimates of Davidson & Ostriker (1973) appeared to be useful for thorough progress in understanding the nature of the observed phenomena. There are the observational features of the accretion-powered X-ray pulsars that need to be explained in the framework of theoretical models embracing as much properties of the real objects as possible. The formation of the spectrum within the polar emitting regions is related with two interesting manifestations (among others): variations in the continuum and in the parameters of the cyclotron resonant scattering feature (CRSF) (Truemper et al. 1978). It is remarkable that the experimental evidences ob-

tained suggest the existence of the relationship between the changes in the continuum and CRSF (Klochkov et al. 2011).

The positive correlation of the CRSF energy with the X-ray luminosity L_X is often associated with the decrease (increase) in the height of the emitting region (being in the inhomogeneous magnetic field of an X-ray pulsar) at increasing (decreasing) L_X (Staubert et al. 2007; Rothschild et al. 2017; Lyutikov & Gavriil 2006). Such a property of the emitting region is often explained (Rothschild et al. 2017; Vybornov et al. 2017; Staubert et al. 2019) by the formation of the gas-dominated accretion column bounded from above by a collisionless shock wave (Bisnovatyi-Kogan & Fridman 1970; Shapiro & Salpeter 1975; Langer & Rappaport 1982; de Hoffmann & Teller 1950). Mushtukov et al. (2015b) proposed the mechanism for the positive correlation related to the Doppler shift of the CRSF during transitions between regimes of a relatively rapid flow and the radiation-dominated accretion column. The negative correlation of the CRSF energy with L_X (Makishima et al. 1990; Tsygankov et al. 2006; Doroshenko et al. 2017; Vybornov et al. 2018) is usually related with the emitting region being in the radiation-dominated regime. However, there is no complete explanation for the phenomenon, and the number of the observed sources demonstrating such a dependence is very small. Possible known interpretations include: variations in the characteristic magnetic field strength due to an increase (decrease) in the height of the emitting region with increasing (decreasing) L_X ; variations in the magnetic field strength within the accretion funnel due to the MHD instabilities (Mukherjee, Bhattacharya & Mignone 2013a); a significant influence on the CRSF position of the intra-atmospheric magnetic field of the neutron star during reflecting the direct radiation from the accretion funnel containing a column of variable height (Poutanen et al. 2013).

The variety of the accumulated observational data on the X-ray continuum of pulsars in a high-luminosity state has also not yet found a complete interpretation. A part of the observations contain the spectra with a fallen power-law tail extending from relatively low energies $\lesssim 10$ keV (Burnard et al. 1991; Becker & Wolff 2007; West et al. 2017b; Becker & Wolff 2022). For some observations, the spectra are characteristic having a high-energy thermal hump, which is sometimes added by a pronounced fallen quasi-power-law tail (Doroshenko et al. 2017; Kong et al. 2022; Shui et al. 2024).

In this work I model the shape of the continuum from the radiation-dominated accretion column of an X-ray pulsar. It is well known that a strongly magnetized plasma is a birefringent medium where the polarized radiation exists in the form of two normal modes (Adler et al. 1970; Canuto, Lodenquai & Ruderman 1971; Ginzburg 1970). The electric vector of one of them, called the extraordinary mode, oscillates mainly perpendicularly to the plane originated by the wavevector and magnetic field direction, and the electric vector of another mode, called the ordinary mode, oscillates mainly in the specified plane. Here, the limit of large Faraday depolarization is considered, which is the case when the modes are orthogonal to high accuracy (Gnedin & Pavlov 1974; Mészáros 1992). The length-scales and magnetic field values (much less than 10^{14} G) within the problem allow using this approximation without concern for the off-diagonal components of the intensity matrix.

The new solutions are numerically obtained within a self-consistent model of an axisymmetrical radiation-dominated accretion column developed in the 3D space (originated by two spatial variables and the photon energy). The calculated dynamical and thermal structures of the column are polarization- and spectrum-dependent. The radiative transfer equations are written in the Fokker-Planck approximation for the extraordinary and ordinary normal modes with the use of frequency-dependent magnetic scattering cross sections. The results include the 2D distributions of the bulk velocity, the electron number density, the total radiation energy density, the electron temperature calculated in the local Compton equilibrium approximation, and related to those distributions of the photon occupation number for both polarization modes. The spectral luminosity of the emergent radiation and, consequently, the polarization fraction are calculated from specified distributions of the occupation numbers.

The basic equations, parameters of the problem and numerical method are described in Section 2. The results are presented in Section 3. The discussion is given in Section 4, and conclusions are contained in Section 5.

2 MODEL SETUP

It will be useful in what follows to consider the flow of plasma accreting on to one of the magnetic poles of a neutron star. Let \dot{M} be the mass accretion rate per magnetic pole characterising this flow. It is supposed that the plasma is purely hydrogen and fully ionized. Since the source of the energy of X-rays from the polar emitting region is the gravitational energy of the accreting matter, a luminosity of the region cannot exceed at a given \dot{M} the value of

$$L \sim \frac{GM\dot{M}}{R}, \quad (1)$$

where M and R are the mass and radius of the neutron star, correspondingly, and G is the gravitational constant. A radiation-dominated mound-like structure forms in the accretion funnel when L exceeds the critical value $L_{\text{cr}} \sim 10^{36} - 10^{37}$ erg s $^{-1}$ (Basko & Sunyaev 1976; Wang & Frank 1981; Becker & Wolff 2007; Mushtukov et al. 2015a). I will consider in detail the mechanisms responsible for the conservation of the kinetic energy of the flow, and consequently for the formation of the structure of the column and the X-ray continuum from the boundary of the funnel.

2.1 Basic equations

Since the shape of the accretion channel is determined by the geometry of the magnetic field, it is useful to introduce spherical polar coordinates (r, θ, ϕ) appropriate to the special situation under consideration (Wang & Frank 1981). The frame is inertial and related with the neutron star, and r is counted from the centre of the star. At the star surface $r = R$. Above the surface r is counted along the magnetic field lines. At the upper boundary of the considered region of the funnel $r = r_{\text{up}}$. The symmetry about the magnetic axis corresponding to $\theta = 0$ is supposed (all quantities are independent of ϕ). Within the funnel, the magnetic field strength $B \sim B_{\text{ns}} r_*^{-1}$, where B_{ns} is the strength at the neutron star

surface, $r_* = r/R$, and l is determined by the shape of the magnetic field lines. Let θ_0 be the angle defined by the side boundary of the filled funnel, and θ_1 and θ_2 be the angles defined by the inner and outer side boundaries of the hollow channel, correspondingly.

The steady state of the accretion column is of interest. The momentum equation reads (Davidson 1973)

$$n_e m_p (\mathbf{v} \cdot \nabla) \mathbf{v} = -\frac{\nabla u}{3}, \quad (2)$$

where \mathbf{v} is the bulk velocity, u is the total mean (angle-averaged) radiation energy density, n_e is the electron number density, and m_p is the proton mass. Equation (2) is written under the assumption that dynamics of the flow is fully determined by the radiation, so that the right-hand side is the radiation pressure gradient accurate to the sign. The gravitational acceleration, the gas pressure, and the viscosity are neglected. The mean total radiation energy density is

$$u = \int_0^\infty u_\epsilon d\epsilon, \quad (3)$$

where $u_\epsilon = 8\pi\epsilon^3 n / (c^3 h^3)$ is the mean spectral radiation energy density, with $n = n_1 + n_2$ is the mode-summed mean photon occupation number, and n_1 and n_2 are the mean photon occupation numbers for the extraordinary (subscript ‘1’) and ordinary (subscript ‘2’) modes (other quantities dependent on the polarization will be denoted in the same way), ϵ is the photon energy, c is the speed of light, and h is the Planck constant. Since the assumption on the frozen plasma is used, the bulk velocity has the only non-zero component $v_r = -v$, where v is the absolute velocity value.

The continuity of the mass flow implies that (Wang & Frank 1981)

$$n_e m_p v r_*^l = \frac{\dot{M}}{A}, \quad (4)$$

where A is the area cut out by the accretion channel at the neutron star surface. In the small-angle approximation, $A = \pi(R\theta_0)^2$ for a filled funnel and $A = \pi R^2(\theta_2^2 - \theta_1^2)$ for a hollow column.

The radiative transfer equations are (Blandford & Payne 1981a; Kompaneets 1956; Mészáros 1992; Gornostaev 2019)

$$\begin{aligned} \nabla \cdot (\hat{D}_i \nabla n_i) - \mathbf{v} \cdot \nabla n_i + \nabla \cdot \mathbf{v} \frac{\epsilon}{3} \frac{\partial n_i}{\partial \epsilon} \quad (5) \\ + \frac{n_e}{m_e c \epsilon^2} \frac{\partial}{\partial \epsilon} \left(\bar{\sigma}_i \epsilon^4 \left(\left(kT + \frac{m_e v^2}{3} \right) \frac{\partial n_i}{\partial \epsilon} + n_i (1 + n_i) \right) \right) \\ + n_e c (\sigma_{i \leftarrow 3-i} n_{3-i} - \sigma_{3-i \leftarrow i} n_i) \\ + \left(\frac{kT}{\epsilon} \right)^3 K_i e^{-\frac{\epsilon}{kT}} \left(1 - n_i \left(e^{\frac{\epsilon}{kT}} - 1 \right) \right) \\ + j_{\text{cyc}, i} = 0, \quad i = 1, 2, \end{aligned}$$

where T is the electron temperature, \hat{D}_i is the diffusion tensor, $\bar{\sigma}_i$ is the angle-averaged scattering cross section, $\sigma_{3-i \leftarrow i}$ is the cross section of the mode switching from the mode denoted by the right-hand subscript, m_e is the electron mass, k is the Boltzmann constant, K_i is the rate of free-free processes, and $j_{\text{cyc}, i}$ is the rate of production of cyclotron photons by means of de-excitations of the first Landau level because of electron-proton collisions. (The i subscript takes everywhere below the values 1 and 2.) Apart

from the mentioned processes of three latter lines of (5), these equations thus describe the spatial diffusion, advection, first-order bulk Comptonization (which attended by the compression of the plasma flow), thermal Comptonization, and second-order bulk Comptonization. The latter is described by adding the $m_e v^2/3$ quantity to the electron temperature within the Doppler term in the Kompaneets operator (Psaltis & Lamb 1997; Titarchuk, Mastichiadis & Kylafis 1997; Farinelli et al. 2012, 2016). (As is known, bulk Comptonization of both kinds is associated with the Fermi processes of the non-thermal nature, ‘accelerating’ photons.)

In the used coordinates, one has $\nabla \cdot \mathbf{v} = \frac{1}{r^l} \frac{\partial}{\partial r} (r^l v_r)$ and

$$\begin{aligned} \nabla \cdot (\hat{D}_i \nabla n_i) = \frac{1}{r^l} \frac{\partial}{\partial r} \left(r^l D_{\parallel, i} \frac{\partial n_i}{\partial r} \right) \quad (6) \\ + \frac{1}{r^2 \sin \theta r_*^{l/2-1}} \frac{\partial}{\partial \theta} \left(\sin \theta D_{\perp, i} \frac{\partial n_i}{\partial \theta} \right), \end{aligned}$$

where the non-zero (diagonal) components $D_{\parallel, i}$ and $D_{\perp, i}$ of the \hat{D}_i tensor describe the diffusion along and across the magnetic field, correspondingly. These are represented as $D_{\parallel, i} = c/(3n_e \sigma_{\parallel, i})$ and $D_{\perp, i} = c/(3n_e \sigma_{\perp, i})$, where $\sigma_{\parallel, i}$ and $\sigma_{\perp, i}$ are the corresponding transport cross sections.

Ignoring the specific behaviour of the electron scattering cross sections near the cyclotron resonance, let us write them for the continuum below the cyclotron energy as (e.g. Canuto et al. 1971; Lodenquai et al. 1974; Arons et al. 1987)

$$\sigma_1 = \left(\frac{\epsilon}{\epsilon_{\text{cyc}}} \right)^2 \sigma_T \quad (7)$$

and

$$\sigma_2 = \left(\sin^2 \alpha + \left(\frac{\epsilon}{\epsilon_{\text{cyc}}} \right)^2 \cos^2 \alpha \right) \sigma_T, \quad (8)$$

where ϵ_{cyc} is the cyclotron energy at a given r , α is the angle between the wavevector of the incoming photon and the direction of the magnetic field, and σ_T is the Thomson cross section. For a medium dominated by the electron scattering (this is the case under consideration, as will be estimated and numerically verified), it is set

$$\begin{aligned} \sigma_{\parallel, 1} = \sigma_{\perp, 1} = \bar{\sigma}_1 = \sigma_{\parallel, 2} = \left(\frac{\epsilon}{\epsilon_{\text{cyc}}} \right)^2 \sigma_T, \quad \sigma_{\perp, 2} = \sigma_T, \quad (9) \\ \bar{\sigma}_2 = \int_0^1 \sigma_2 d \cos \alpha = \frac{1}{3} \left(2 + \left(\frac{\epsilon}{\epsilon_{\text{cyc}}} \right)^2 \right) \sigma_T. \end{aligned}$$

The mode switching cross sections are written, taking the angle-averaged value for the ordinary mode, as

$$\sigma_{3-i \leftarrow i} = \frac{1}{4} \left(\frac{\epsilon}{\epsilon_{\text{cyc}}} \right)^2 \sigma_T. \quad (10)$$

For the photon energies above the cyclotron energy, it is set that $\sigma_{\parallel, i} = \sigma_{\perp, i} = \bar{\sigma}_i = \sigma_T$, and $\sigma_{3-i \leftarrow i} = \sigma_T/4$. The use of a factor of one third in the spatial diffusion coefficients is a certain arbitrariness, which cannot lead to any errors in the solutions within the problem under consideration, except for an insignificant variation in the width of the shock wave not affecting the spectrum of the funnel.

The rate of free-free interactions for the ordinary mode is well approximated in the continuum by the non-magnetic

formula (Karzas & Latter 1961; Illarionov & Syunyaev 1975a)

$$K_2 = \frac{8\pi}{3} \frac{e^6 h^2}{\sqrt{6\pi} m_e^3} n_e^2 (kT)^{-\frac{7}{2}} g\left(\frac{\epsilon}{kT}\right), \quad (11)$$

where e is the electron charge, and

$$g(x) = \begin{cases} 1, & x \geq 1, \\ \frac{\sqrt{3}}{\pi} \ln \frac{2.35}{x}, & x < 1 \end{cases} \quad (12)$$

is the Gaunt factor written with the use of the Born approximation for an arbitrary x . It is set that $K_1 = 0$, since the coefficients of the free-free absorption and emission for the extraordinary mode in the continuum are several orders of magnitude smaller compared to those for the ordinary mode at the energies of interest (e.g. Nagel 1981; Suleimanov et al. 2022).

Simple estimates for a non-magnetized static medium show that the Compton scattering is a much more efficient mechanism of the energy exchange than free-free processes in the problem under consideration. Indeed, the corresponding rate of the Compton interactions is (Illarionov & Syunyaev 1975a)

$$a \sim \frac{kT}{m_e c} \sigma_T n_e, \quad (13)$$

and the rate of free-free processes is (cgs)

$$K \sim 1.2 \times 10^{-12} n_e^2 T^{-\frac{7}{2}} \quad (14)$$

for $\epsilon > kT$. In the considered parameter ranges, for both geometries a significantly exceeds K throughout the column. Consequently, the heating and cooling due to Compton scatterings are the main processes governing the electron temperature within the settling mound (post-shock zone in the velocity distribution) and the dense region of the shock wave.

The source of cyclotron photons is given (cgs) by the expression (Arons et al. 1987; Becker & Wolff 2007)

$$\sum_i j_{\text{cyc}, i} = 1.8 \times 10^{-60} \epsilon^{-2} n_e^2 B_{12}^{-\frac{3}{2}} H\left(\frac{\epsilon_{\text{cyc}}}{kT}\right) e^{-\frac{\epsilon_{\text{cyc}}}{kT}} f, \quad (15)$$

where $B_{12} = B/10^{12}$ G,

$$H(x) = \begin{cases} 0.41, & x \geq 7.5, \\ 0.15\sqrt{x}, & x < 7.5, \end{cases} \quad (16)$$

and

$$f = \delta(\epsilon - \epsilon_{\text{cyc}}). \quad (17)$$

In the computations, the delta function is approximated by the normalized Gaussian function

$$f = \frac{1}{\sqrt{2\pi}\tilde{\zeta}} e^{-\frac{1}{2}\left(\frac{\epsilon - \epsilon_{\text{cyc}}}{\tilde{\zeta}}\right)^2}, \quad (18)$$

where $\tilde{\zeta} = \zeta/1$ keV = 1 (e.g. Farinelli et al. 2016; West et al. 2017b). Normalization is formally used for the infinite range of the variable, since the distribution is centred far from zero. Using normalization for the semi-infinite range does not affect the results remarkably. It is assumed that $j_{\text{cyc}, 1} = j_{\text{cyc}, 2}$.

The local Compton equilibrium temperature (the Compton temperature) gives the value of the electron temperature in a medium when this value is determined by the

spectrum of the radiation. For the case of a non-polarized radiation in a static medium, the Compton temperature reads (Zel'dovich & Levich 1970)

$$T_{\text{C, np}} = \frac{\int_0^\infty \epsilon^4 n_{\text{np}} (1 + n_{\text{np}}) d\epsilon}{4k \int_0^\infty \epsilon^3 n_{\text{np}} d\epsilon}, \quad (19)$$

where n_{np} denotes the corresponding photon occupation number. Multiplying this expression by the denominator, writing the resulting expression for each mode and summing equations, one can obtain

$$T_{\text{C}} = \frac{\int_0^\infty \epsilon^4 \sum_i n_i (1 + n_i) d\epsilon}{4k \int_0^\infty \epsilon^3 n d\epsilon}. \quad (20)$$

To describe the thermal structure of the funnel, it can be then supposed

$$T = \begin{cases} T_{\text{C}} - \frac{m_e v^2}{3k}, & T_{\text{C}} - \frac{m_e v^2}{3k} \geq T_*, \\ T_*, & T_{\text{C}} - \frac{m_e v^2}{3k} < T_*, \end{cases} \quad (21)$$

where the constant T_* is the electron temperature set in the region in which the temperature value cannot be fully governed by the radiation. This is the case of the pre-shock region and the upper low-density region of the shock wave, where too low values of the photon number density and too high values of the bulk velocity make the local Compton equilibrium approximation inapplicable. Since an exact calculation of the electron temperature in this region is not the goal of this work and cannot change the main results, (21) is used in the simulations. The influence of plasma compression on the temperature manifests mostly through the values of the photon occupation numbers, and the effects, which would come through the modification of the expression for the temperature, are negligible. Expressions (19) and (20) also do not include the terms responding to free-free processes. After equating the heating and cooling rates, it can be shown that the inclusion of these terms in (19) and (20) could affect the values of $T_{\text{C, np}}$ and T_{C} at plasma densities considerably exceeding those at which the gas pressure becomes important.

The momentum equation and the radiative transfer equations require boundary conditions. As a boundary condition for equation (2), it is set that

$$v(r_{\text{up}}) = v_{\text{ff}}(r_{\text{up}}) = \sqrt{\frac{2GM}{r_{\text{up}}}}, \quad (22)$$

where v_{ff} denotes the free-fall velocity, or $v(r_{\text{up}})$ is set to be equal to a certain value. For the transfer equations, at the upper boundary it is set

$$n_i(r_{\text{up}}) = 0. \quad (23)$$

The free escape of the photons is supposed at the sidewall (sidewalls), so that

$$-\frac{D_{\perp, i}}{r} \frac{\partial n_i}{\partial \theta} \Big|_{\theta=\theta_0} = \frac{2}{3} c n_i(\theta_0) \quad (24)$$

for the filled funnel and

$$(-1)^d \frac{D_{\perp, i}}{r} \frac{\partial n_i}{\partial \theta} \Big|_{\theta=\theta_{d+1}} = \frac{2}{3} c n_i(\theta_{d+1}), \quad d = 0, 1 \quad (25)$$

for the hollow funnel. It is supposed that the blackbody spectrum is established at the bottom, so that

$$n_i(R) = \frac{1}{2} \left(e^{\frac{\epsilon}{kT_0}} - 1 \right)^{-1}, \quad (26)$$

where

$$T_0 = \left(\frac{3\gamma\dot{M}v(r_{\text{up}})}{Aa_r} \right)^{\frac{1}{4}}, \quad (27)$$

with a_r is the radiation energy density constant and $\gamma \approx 1 - v(R)/v(r_{\text{up}}) \sim 1$ is the parameter (in the uniform magnetic field $\gamma = 1 - v(R)/v(r_{\text{up}})$). For the filled column

$$\left. \frac{\partial n_i}{\partial \theta} \right|_{\theta=0} = 0. \quad (28)$$

At the boundaries of the photon energy domain corresponding to $\epsilon_1 = 0.07$ keV and $\epsilon_2 = 500$ keV it is set that

$$n_i(\epsilon_1) = n_i(\epsilon_2) = 0. \quad (29)$$

Regarding the boundary conditions for the transfer equations, it should be noted that the top boundary is different from the side ones, since there is no any real physical boundary of the medium at the top (the structure of the flow up to the magnetospheric boundary is not discussed here). Relatively low-intensity spectrum taking place not so far from that boundary cannot be simply an additive contribution to the outgoing radiation. A lot of the photons forming that spectrum – sooner or later – get knocked down and thus became a contribution to the sidewall emission, which is determined by solving the spatially 2D radiative transfer under the conditions of the funnel. The radiation flux along the magnetic field vanishes at large r . The spectrum of radiation emerging from the channel above the set upper boundary can be found by modelling the radiative transfer in the corresponding spatial regions.

The substantially non-stationary situation near the column base cannot be simulated in detail while one is constrained by the considered system of equations, therefore the values of the electron number density obtained for the corresponding region may differ from real those.

2.2 Problem parameters

The value of $\dot{M}_{17} = \dot{M}/10^{17} \text{ g s}^{-1}$ is varied in the range 0.2–5. It is always set that $\epsilon_{\text{cyc}}(R) = 50$ keV.

The radius of the funnel base depends on the accretion rate. The angular half-width of the funnel base $\theta_0(\dot{M}_{17} = 1)$ is taken as a parameter of the problem for a filled funnel, while $\theta_1(\dot{M}_{17} = 1)$ and $\theta_2(\dot{M}_{17} = 1)$ are parametrized for a hollow funnel. It is supposed that $\theta_2 = 1.1\theta_1$ and $\theta_1 = \theta_0$, with $\theta_0 = \theta_0(\dot{M}_{17} = 1)\dot{M}_{17}^{1/7}$ (Lamb, Pethick & Pines 1973; Shapiro & Teukolsky 1983). The angular width of the funnel base is not strictly related to the value of the surface magnetic field. It is set that $\theta_0(\dot{M}_{17} = 1) = 0.08$ (one would exclude the parameters θ_0 , θ_1 and θ_2 , and set them as some functions of B_{ns} and \dot{M} for a given neutron star).

It is set that $M = 1.4M_{\odot}$ and $R = 10^6$ cm. In what follows, the case of $l = 3$ corresponding to the dipole magnetic field is considered. It is supposed that $T_* = 1$ keV, which is of the order of magnitude equal to the real electron temperature in the flow above the emitting region. It is set that

$\gamma = 0.98$. The $v(r_{\text{up}})$ quantity is considered as a parameter in the particular case, where $v(r_{\text{up}}) = 1.3 \times 10^{10} \text{ cm s}^{-1}$.

Higher values of the mass accretion rate as well as distinct values of the surface magnetic field strength, the radius of the funnel base and the thickness of the filled part of the hollow funnel will be considered in a separate paper.

2.3 Numerical approach

Computations are performed with the use of the time-relaxation method. The initial spectrum in the medium is the Wien distribution for the temperature of 1 keV. At each time step, to find the velocity with the use of (2) at a given point in space for some spectral distribution, the total radiation energy density is determined by expression (3). The electron number density is eliminated in (2) with the use of (4). After integrating the momentum equation, the electron temperature is found with the use of (21) over the entire computational domain (the Stefan-Boltzmann law is not used anywhere except for calculating the value of T_0).

To find the photon occupation number at each time step, an explicit finite-difference scheme developed by G2021 is used, with additions and modifications related to the physical picture of the problem and aimed at the approximation of the radiative transfer equations (5) in their specific form considered here. There is no the sense to write out the dimensionless form of the equations, since the example of such a representation can be found by the reader in the mentioned paper (the grids are similar with accuracy to the steps used). For a given i , the term describing thermal and second-order bulk Comptonization is rewritten after performing differentiation as a sum of terms, each of which contains a derivative of the dimensionless spectral radiation energy density of only one order or does not contain its derivatives of an order higher zeroth. These terms are approximated, as well as the advection and first-order bulk Comptonization terms, according to the typical rules (Press et al. 1992; Samarskii 2001; Kalitkin 1978). The terms containing the derivatives of the cross sections $\bar{\sigma}_i$ with respect to ϵ are taken into account. In each transfer equation, the n_i^2 nonlinearity originates three monomials, one of which contains the product of the dimensionless spectral radiation energy density and its first derivative approximated by the central difference, and the others contain the specified function squared. To approximate the spatial diffusion terms (see (6)), the pattern functionals containing the arithmetic means (Samarskii 1962) are basically used – the results are nearly identical to those obtained by means of the approximation after differentiation of the brackets.

The codes for simulating the accretion columns were written in C and executed in parallel with the use of OpenMP. The calculations were performed using total capabilities of two 56-core (AMD EPYC 7663) CPUs. The overall compute time of the presented simulations is about three months.

3 RESULTS

3.1 Accretion column in the radiation-dominated regime

The dynamical picture of the problem is known. Consider a freely falling flow. Let X-ray photons be generated at the base of the funnel, and let their total luminosity be determined by the expression (1) (a separate consideration of the case when photons are produced in the region of a certain height above the atmosphere is omitted). An increase in the accretion rate and the X-ray luminosity causes an increase of the role of the pressure of the radiation propagating upwards. The flow begins to slow higher up, and the X-ray photons escaping the funnel begin to partially gain the energy in the appearing region of small values of $|\nabla \cdot \mathbf{v}|$, and even somewhat above it, in the near-divergence-free flow. A further increase in the accretion rate provides an increase in the fraction of photons gaining considerable energy in the shock wave and thus an increasingly sharp convergence of the flow. Once a sufficiently strong shock wave is formed, the settling mound begins to arise, as a significant portion of the photons penetrate beneath the shock. The seed free-free radiation is always originated mostly inside the underlying atmosphere. Photons appeared inside the settling mound accomplish random walks before escaping after a time equal on average to the mean diffusion time for the mound. As the accretion rate increases further, the shock wave becomes steeper and the peak height of the deceleration zone grows. Both effects occur (up to achieving some state), since the profile of the shock wave must provide the illumination of the radiation for a given accretion luminosity. A relatively small part of the pre-shock kinetic energy of protons is converted into the thermal energy of electrons. Within the shock, there is a surface where the supersonic decelerating flow becomes subsonic (the speed of sound in a radiation-dominated plasma is $c_s = 2/3\sqrt{u/(m_p n_e)}$).

The spectrum of the radiation in the column is almost entirely determined by the Compton energy exchange between electrons and photons. Modelling the radiative transfer in the hot rarefied plasmas in the presence of a strong magnetic field leads to results for the emergent spectrum distinguishing from those for a nonmagnetized medium, mainly in the consequence of the dependence of the differential scattering cross sections on polarization, frequency, directions of propagation of incoming and outgoing photons, magnetic field strength, electron temperature and mass density (Mészáros 1992). The dependence of the cross sections on the electron temperature is of importance mostly for modelling the radiative transfer in the vicinity of cyclotron resonances, whose broadening is more remarkable, the higher the electron temperature. The Compton y -parameter characterising thermal Comptonization in the continuum (e.g. Rybicki & Lightman 1979) is reduced considerably compared to the nonmagnetic value for both modes at frequencies well less than the cyclotron frequency. Even for values of the nonmagnetic y -parameter much exceeding unity, under the conditions of the hard thermal backlight and static isothermal medium, magnetic Comptonization can cause an emergent spectrum summed over the modes, which has a nearly power-law shape at high frequencies. The general description of Comptonization in strongly magnetized plasmas is

rather complicated and remains beyond the scope of this paper.

Geometrically 2D models of the radiation-dominated accretion column differ from 1D models by that the 2D model settling zone is surrounded by the shock wave and, thus, completely submerged in the flow, so that there is no direct path between that zone and the outer space. Such models should be of interest in light of finding their relationship to observational data.

The model developed here is applicable for values of the parameters which provide at least the very beginning of originating the settling zone. For the total luminosity of two identical columns one can write that

$$L_X \sim \dot{M} v^2 (r_{\text{up}}). \quad (30)$$

For the case of a freely falling pre-shock flow one has $L_X \approx 2L$. At reasonable choice of r_{up} expression (30) characterises approximately, in principle, any emitting region regardless that whether it being in the radiation-dominated state or not. The specific of the radiation-dominated column is that the temperature T_0 is relatively higher than calculated for the same parameters the effective temperature of the hot spot

$$T_{\text{eff}} \approx \left(\frac{\dot{M} v^2 (r_{\text{up}})}{2Ab} \right)^{\frac{1}{4}}, \quad (31)$$

where b is the Stefan-Boltzmann constant. The ratio of the temperatures is

$$\frac{T_0}{T_{\text{eff}}} \approx \left(\frac{3}{2} \frac{c}{v(r_{\text{up}})} \right)^{\frac{1}{4}}. \quad (32)$$

That is, the processes characteristic for the shock wave provide more effective heating of the medium than that would take place in a ‘pure thermal’ atmosphere.

3.2 Results of the numerical calculations

The solutions to system of equations (2), (3), (4), (5) and (21) with boundary conditions (22), (23), (24), (26), (28) and (29) (or (25) instead of both (24) and (28)) are considered. The main results of the current simulations are shown in Figs 1–4. The local spectrum throughout the column is plotted in terms of the spectral radiation energy density in some points. The spectral luminosities L_{ϵ} , $L_{\epsilon, i}$ represent the sidewalls-integrated emergent continuum, and the polarization fraction is defined as

$$\text{PF} = \frac{L_{\epsilon, 2} - L_{\epsilon, 1}}{L_{\epsilon, 1} + L_{\epsilon, 2}}. \quad (33)$$

The boundaries of the colour bars related to the 2D distributions approximately indicate the minimum and maximum values approached within the shown domains (for the velocity, these values fall within the corresponding boundary intervals). The difference between θ_0 , θ_1 and θ_2 in calculations and their values indicated above lies within the grid steps. Seediness at the front of the shock wave in the electron temperature distributions is the trace of the colour interpolation and is neither a manifestation of the scheme instabilities nor a property of the grid functions.

For a filled funnel $r_*(r_{\text{up}}) = 1.2$ ($L_{X, 37} \approx 3.1$ for $M_{17} = 1$, $L_{X, 37} \approx 9.3$ for $M_{17} = 3$, and $L_{X, 37} \approx 15.6$ for

$\dot{M}_{17} = 5$), where $L_{X,37} = L_X/10^{37} \text{ erg s}^{-1}$. In the case of a hollow funnel $r_*(r_{\text{up}}) = 1.007$ ($L_{X,37} \approx 3.7$ for $\dot{M}_{17} = 1$). The luminosity is given here for $v(r_{\text{up}}) = v_{\text{H}}(r_{\text{up}})$. The spectral luminosity shown below for a hollow funnel is calculated as the sum of the luminosities of the side boundaries. The labels ‘ $u_{\epsilon,i}$ ’ and ‘ $L_{\epsilon,i}$ ’ are dropped in the figures.

The self-consistent approach used allows to simulate a specific profile of the shock wave corresponding to the frequency dependence of the cross sections for a given $B(r)$ and to the local spectrum formed. The calculated characteristic values of $\nabla \cdot \mathbf{v}$ correspond approximately to those obtained in the grey approximation for rather large cross section along the magnetic field $\sim 0.3\sigma_{\text{T}} - \sigma_{\text{T}}$ (e.g. Davidson 1973). The growth of the column slows down as the accretion rate increases in the considered range of its values mainly due to the frequency dependence of the cross sections along the magnetic field. The growth virtually comes out to the saturation taking place at \dot{M}_{17} in the range 3–5 (Figs 2 and 3). The vertical widening of the flow in the non-uniform magnetic field, and the effects of the frequency photon redistribution and the heating of the plasma always make the dependence of the height of the mound on the accretion rate less steep compared to the simple solutions of Postnov et al. (2015), but do not lead to its strong slowing down at $\dot{M}_{17} \gtrsim 1$ being taken into account under the grey approximation.

The polarimetric spectrum demonstrates typically an excess of the radiation of the extraordinary mode at energies near the maximum of the spectrum of that mode and prevailing the ordinary mode at high energies. The dependence of the radiation flux on the photon energy at low energies $\propto \epsilon^2$ is always the same for both modes. At low accretion rates, the emergent spectra of both modes have the maximums at energies not exceeding strongly the value $\sim kT_0$. With increasing accretion rate, the shape of spectrum of the extraordinary mode varies insignificantly at low energies with hardening the tail, while the spectrum of the ordinary mode gradually tends to saturation. The high-energy tails are formed by the effects of bulk motion and thermal Comptonization. While the spectrum of the ordinary mode is quite far from saturation, the frequency behaviour of the used cross sections causes that the total spectrum falls steeply below the ‘averaged’ cyclotron line energy which thus manifests in the absence of resonance in the cross sections. In the spectrum of the extraordinary mode that feature is held for any \dot{M} . It should be modified in exactly calculated spectra by the cyclotron line and wings of the line.

The growth of the accretion rate from $\dot{M}_{17} = 1$ to $\dot{M}_{17} = 5$ causes a decrease in the spectral hardness calculated as the ratio of the luminosity in the range 5–12 keV to luminosity in the range 1–3 keV with increasing \dot{M} with going out to an almost constant.¹ A softening occurs as the relative contribution of the ordinary mode to the luminosity decreases in the range 5–12 keV faster than in the range 1–3 keV during a tending to the saturation of the spectrum of the ordinary mode (a hardening of the total spectral tail) at increasing \dot{M} and fixed other parameters.

¹ The similar energy ranges were used in the analysis of Postnov et al. (2015). The minimum and maximum energies are close to the boundaries of the *RXTE*/*ASM* energy band.

It follows from the description above that, in simulations, the absolute values of PF increase with increasing accretion rate (Figs 1–3). That is, unsaturated Comptonization of the radiation of the ordinary mode can result in an emergent spectrum comparably close to the spectrum of the extraordinary mode (at least at $\dot{M}_{17} \lesssim 1$, Figs 1, 4, 5 and 6). It is especially clear in the case of the near-critical value of the accretion rate $\dot{M}_{17} = 0.2$ ($r_*(r_{\text{up}}) = 1.15$, $L_{X,37} \approx 0.7$), see Fig. 6. The calculated PF in the range 1–20 keV is in a satisfactory agreement with theoretical that of Burnard et al. (1991) and with characteristic observational values (e.g. Tsygankov et al. 2022; Long et al. 2023).

The first vacuum frequency (Ventura, Nagel & Meszaros 1979) falls in the soft X-ray range in the considered cases. Hence the potential effect of the conversion of the cross sections between the vacuum frequencies is trivial and reduces to recalling the spectra of the modes above the first vacuum frequency.

3.3 Effects of induced scattering and of the magnetic field geometry

The present simulations self-consistently show that in general the influence of the induced Compton effect on the structure of the accretion column and the radiation spectrum in the funnel cannot be neglected. Inside the settling mound, far enough from the shock wave, Compton scatterings establish a state close to LTE, with induced scattering can play a notable role. That is, in the specified region one has

$$T \approx T_C \sim \left(\frac{u}{a_r} \right)^{\frac{1}{4}} \sim T_0, \quad (34)$$

as it could be expected based on the smallness of the radiation flux there. The total local spectrum can be rather close to the Planck spectrum or have a characteristic saturated form in this region, but approach neither the Planck nor the Wien distribution. In the latter case, the spectrum has a zone of less steep slope than in the Rayleigh-Jeans range (e.g. Figs 2, 3 and 7).

Fig. 8 shows the results for the electron temperature in the filled funnel along the magnetic axis and for the corresponding emergent spectrum (cf. Zel’dovich & Illarionov 1974; Klein et al. 1996), obtained in a geometrically 2D domain under the grey approximation analogously to the calculations of G2021 (section 3, the system of equations includes the only transfer equation), but with taking into account the induced Compton effect, second-order bulk Comptonization, free-free processes with the use of (11), the cyclotron emission with the use of (15), and the dipole geometry of the magnetic field. The scattering cross section along the magnetic field equal to $0.1\sigma_{\text{T}}$ is used. Such calculations being performed without taking into account the induced Compton effect do not show an agreement of the dependencies for the model Compton temperature in the settling mound (Fig. 8) with the Stefan-Boltzmann law. Neglecting free-free processes leads to an additional decrease in the model Compton temperature. This is in accordance with its values ~ 0.2 – 2 keV (at the typical radiation energy density of about 2.6×10^{17} – $4 \times 10^{17} \text{ erg cm}^{-3}$, which is nearly constant throughout the settling zone) appeared in the results of G2021 (figs 5 and 6), which thus contain the spectra

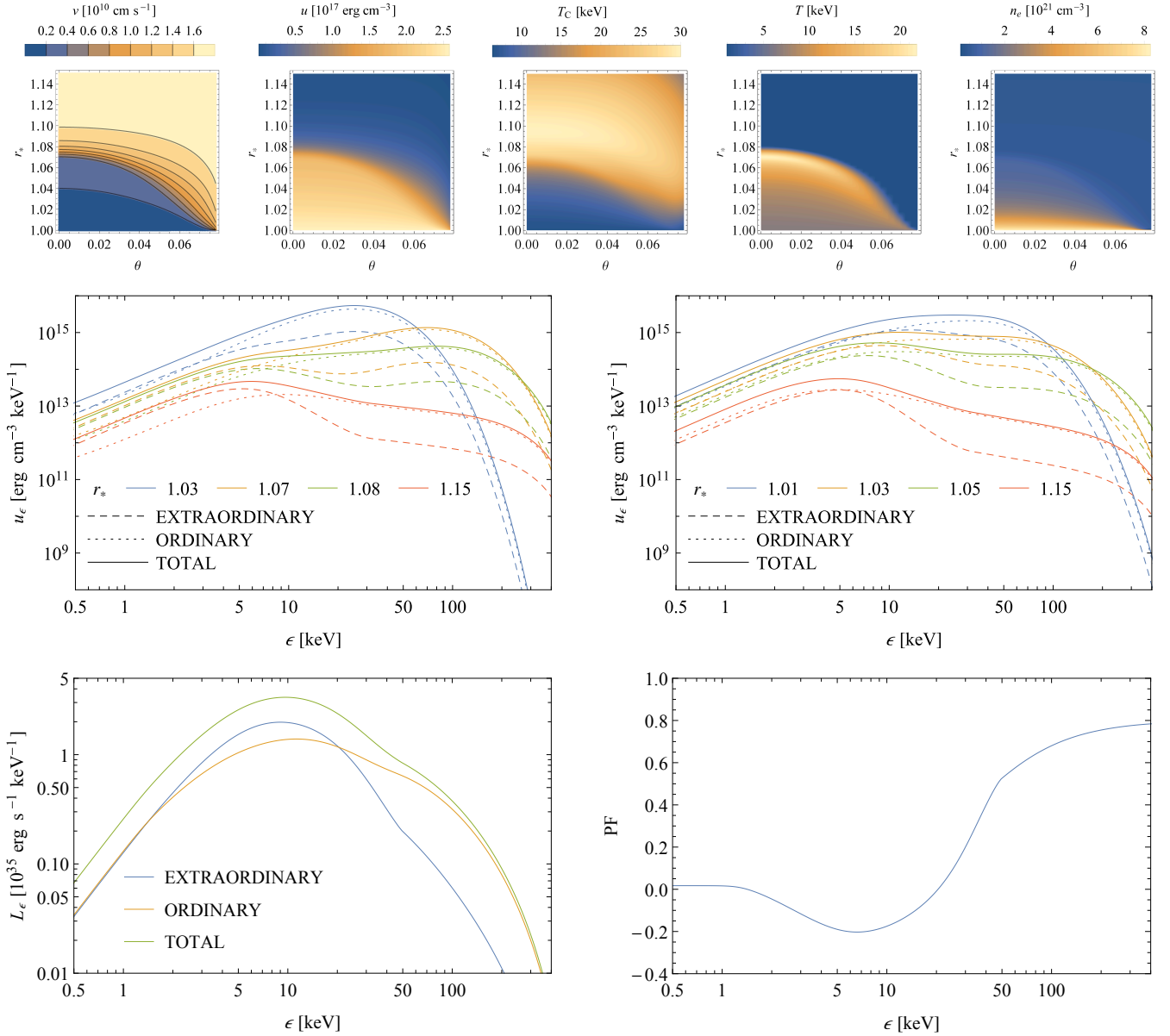


Figure 1. Column grown in the filled accretion funnel, calculations for $\dot{M}_{17} = 1$: (top panels) the structure, (middle) the spectrum of the radiation in the number of points within the funnel, (left) $\theta = 0$ and (right) $\theta = 0.07$, (bottom left) the spectral luminosity of the radiation from the side boundary of the funnel, and (bottom right) the polarization fraction for the emergent radiation.

of a shock wave itself with a soft backlight (cf. Lyubarskii & Syunyaev 1982).

The grey approximation allows thus modelling a local situation in the column that would be rather close to a situation without a strong magnetic field at least accurate to the details of the shock profiles. It is justified regardless of the value of the scattering cross section along the magnetic field (as long as that value is not too small), the value of the cyclotron emission term and the values of other parameters. That is, in a sufficiently weak magnetic field, induced scattering is of great importance for establishing of the electron temperature in the interiors of the settling mound. In this case, the value of T is very close to the LTE values throughout the whole zone behind the temperature shock.

It turns out that thermal Comptonization cannot pro-

vide the existence of a satisfactory self-consistent steady-state solutions while the induced Compton effect is ignored, except for some special cases corresponding usually to relatively low accretion rates $\dot{M}_{17} \lesssim 2$. The decrease in the angle-averaged scattering cross sections with frequency in both modes causes that in a sufficiently strong magnetic field, in the models without allowance for induced scattering (when a solution exists), the model photons lose the energy in the settling mound slowly, therefore the deficit in the electron temperature relative to the exact solutions is not dramatic for those models and can approach no much than ~ 1 keV even for the solutions not accounting for the free-free processes (Fig. 9).

The value of u in the settling zone decreases with increasing r the slower, the lesser the l quantity. The mound

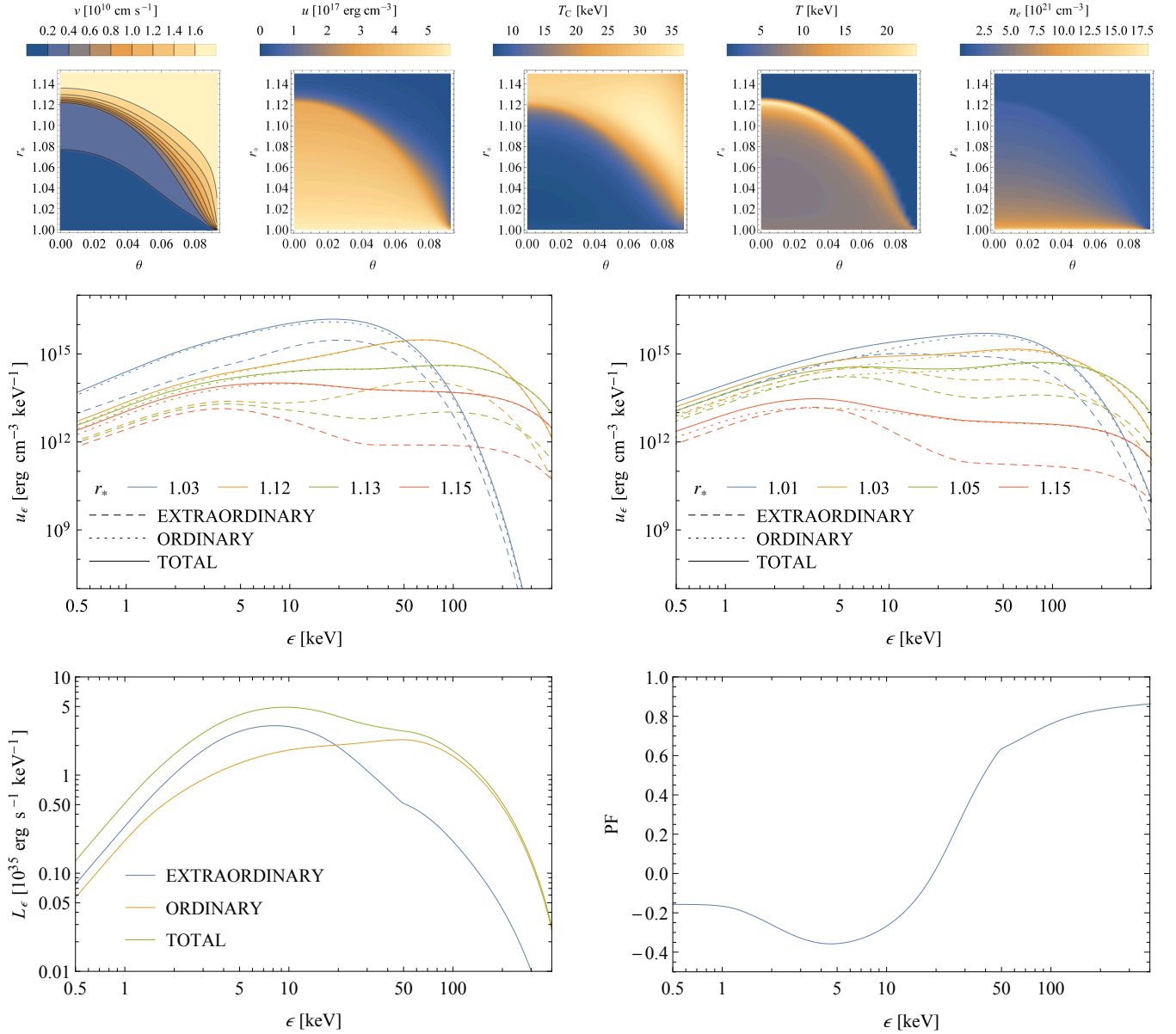


Figure 2. Same as Fig. 1, but for $\dot{M}_{17} = 3$. In the right panel, the spectral radiation energy density is shown for $\theta = 0.087$.

is lower than in the cylindrical channel at the same parameters (the area of the transverse cross section of the cylindrical channel is assumed to be equal to the area of the funnel base). The radiation flux component along the magnetic field differs from zero in the interiors of the settling mound, consequently, mostly due to the geometry of the magnetic field.

Within the shock wave, the effect of induced scattering is insignificant at any magnetic field, since the n_i quantities are small at the large radiation fluxes. The influence of the anisotropy of the photon occupation numbers, which is mostly determined by the squares of those and by the coordinate, should not then change the results for the electron temperature strongly (Levich & Sunyaev 1970).

Taking into account the induced Compton effect in the radiative transfer treatments was performed earlier in the

framework of static models of emitting regions (Meszaros, Pavlov & Shibano 1989; Alexander, Meszaros & Bussard 1989).

3.4 Effects of bulk Comptonization

The thermal structure of the shock differs from the settling region mainly because of the influence of first-order bulk Comptonization (compressional ‘acceleration’ of photons) (Blandford & Payne 1981a,b). This is one of the mechanisms in addition to the thermal Doppler effect, which supplies photons at high energies and causes the heating of the plasma due to the recoil in the region of great values of $|\nabla \cdot \mathbf{v}|$ to electron temperatures considerably exceeding the values of the $(u/a_r)^{1/4}$ quantity and the value of T_0 .

Second-order bulk Comptonization occurs mostly in the

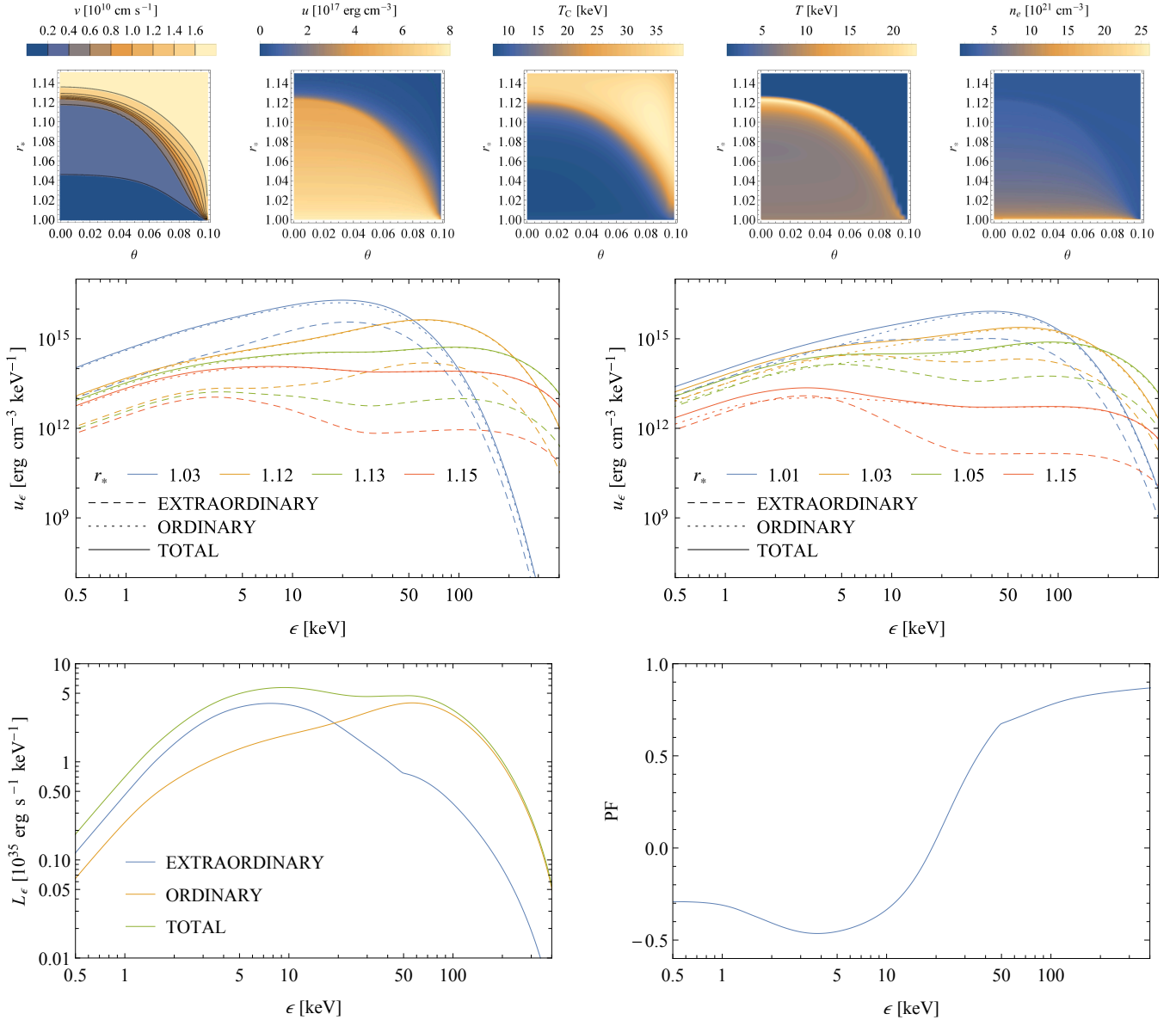


Figure 3. Same as Fig. 1, but for $\dot{M}_{17} = 5$. In the right panel, the spectral radiation energy density is shown for $\theta = 0.093$.

upper, relatively cold layers of the shock wave and in a rather narrow low-intensity layer of the pre-shock region from where the radiation is still capable of contributing to the emergent flux. In principle, it is possible to model approximately the structure of the shock by solving self-consistently the transfer equations of sort of equations (5), ignoring both thermal and second-order bulk Comptonization – in such solutions the emergent spectra of both modes have the power-law tails, which is in accordance with the results of Blandford & Payne (1981b) and Becker & Wolff (2005).

Compared to the results where second-order bulk Comptonization is neglected, the peak height of the calculated shock above the neutron star surface is relatively larger (the typical difference is described by a factor of 2), while the calculated electron temperature in the shock wave is relatively higher (and typically differs by 1.5–2 times), which

indicates the increase in the density of hard photons (forming eventually the tail of the spectrum of the funnel). The quantities T and $T + m_e v^2 / (3k)$ become almost equal at the value of r (at a given θ) at which the value of T approaches its maximum. The corresponding contour is close to the inner boundary of the shock wave. Above that contour, one can distinguish another level where the dominance of the $m_e v^2 / 3$ term is relieved by the dominance of the electron temperature. An excess of hard photons in the upper part of the settling mound manifests in a spreading of the inner boundary of the temperature shock or (in relatively weak fields) in a smaller altitude of this boundary in comparison to the velocity shock. The T_C quantity approaches a maximum in the outer layers of the shock, which indicates that as the hard radiation penetrates against the accretion flow into the region above the shock wave, losing in the photon number density.

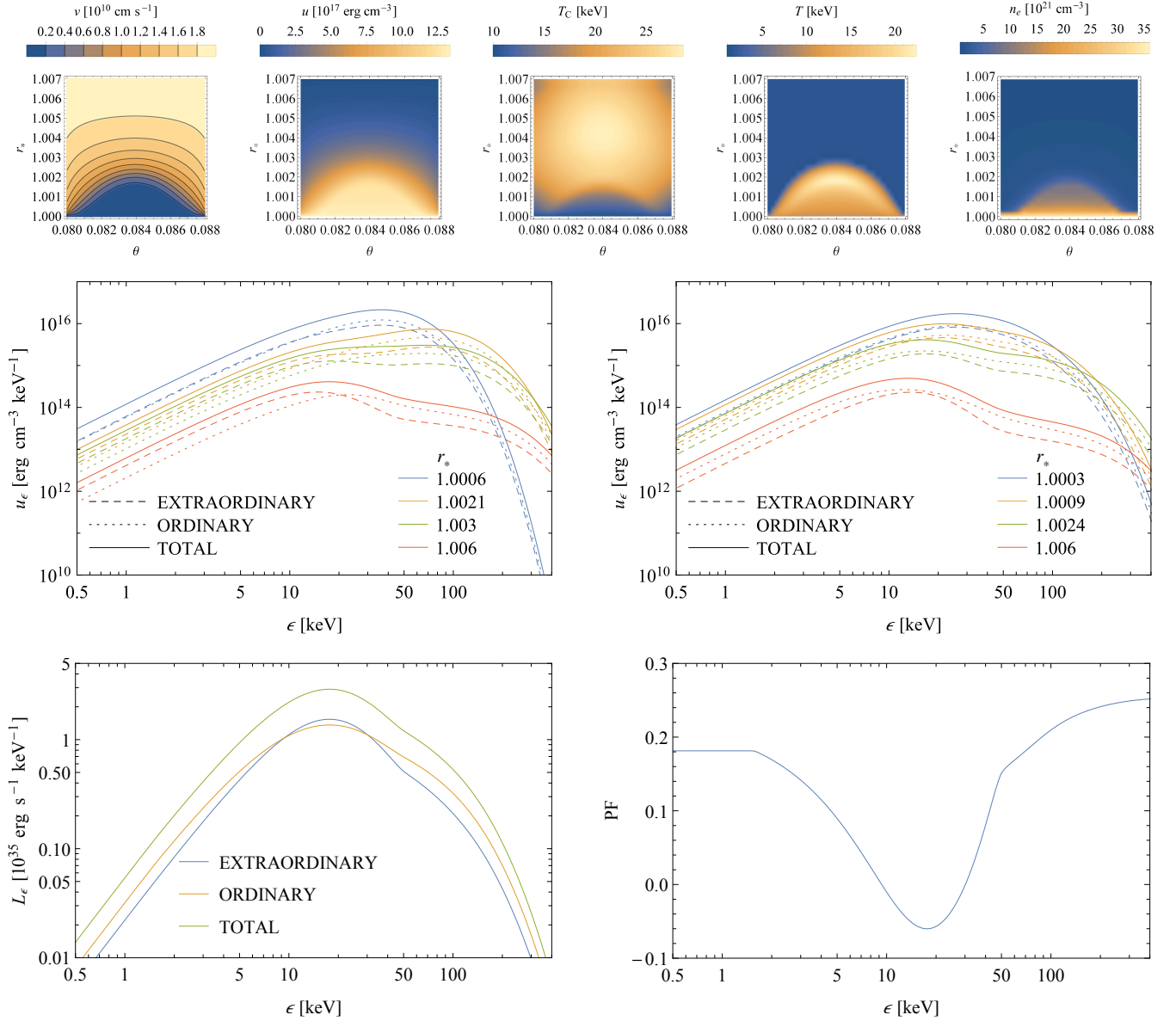


Figure 4. Same as Fig. 1, but for the hollow funnel. The spectral radiation energy density is shown for (left) $\theta \approx (\theta_1 + \theta_2)/2$ and (right) $\theta \approx 0.0875$.

In the absence of a magnetic field, first-order bulk Comptonization would be the reason of a shift in the maximum of the emergent spectrum towards higher energies relative to the characteristic energy $2.8kT_0$. This is a typical picture (see Psaltis & Lamb 1999, fig. 1). In a strong magnetic field this effect takes place as well. The emergent spectrum of the extraordinary mode is shifted to higher energies relative to the value of kT_0 mainly due to the influence of first-order bulk Comptonization, while the thermal effect of the shock wave is not very significant for the shift. The spectrum of the ordinary mode can be affected by the heating of the shock wave. If a high-energy hump in the emergent spectrum of the ordinary mode is formed, it usually corresponds to the energy $\sim 2kT_s$, where T_s is the maximum electron temperature (approaching in the shock wave).

Thus, second-order bulk Comptonization leads to an in-

crease in the intensity in the high-energy tails (both directly and through the heating of the medium) compared to the tails formed by first-order bulk and thermal Comptonization. The high-energy tail of the total spectrum of intensities well above those of the extraordinary mode is formed as well in the framework of self-consistent calculations with an artificially cooled shock wave to a temperature of T_0 or to a temperature taken to be equal to $(u/a_r)^{1/4}$. The high column in such simulations is not formed, so that the resulting ‘shock wave’ lies on the neutron star surface – this shows that the heating of the shock wave at least in the correspondence with solutions of G2021 is the necessary condition for the formation of the dynamical structure (in contrast to the heating of the post-shock zone).

The influence of the $m_e v^2/3$ term can be illustrated by varying the velocity at the upper boundary. Con-

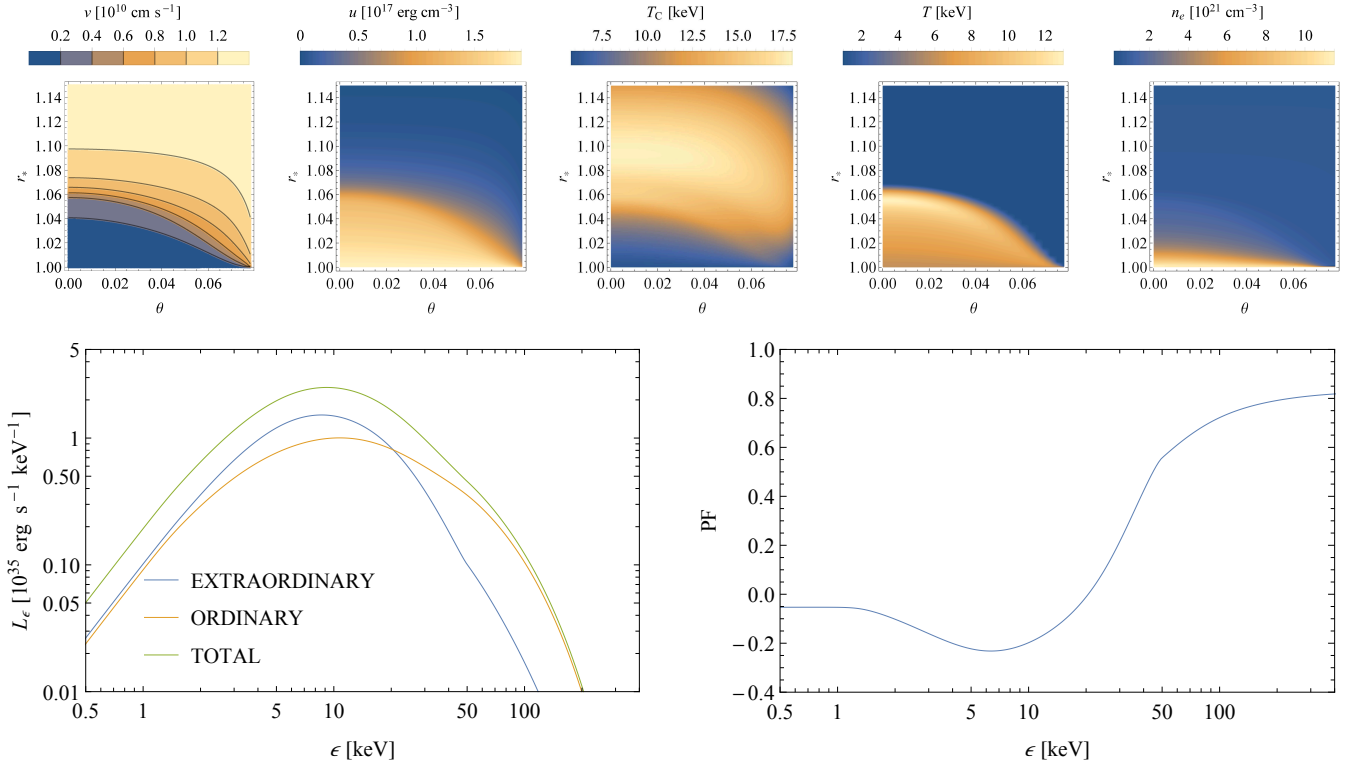


Figure 5. Same as Fig. 1, but for $v(r_{\text{up}}) = 1.3 \times 10^{10}$ cm s $^{-1}$ (panels for the local spectra are not shown).

consider a filled funnel. In Fig. 5 the structure, the emergent spectra and the polarization fraction are shown for $v(r_{\text{up}}) = 1.3 \times 10^{10}$ cm s $^{-1}$ ($\dot{M}_{17} = 1$, $L_{X,37} \approx 1.7$). The decrease in $v(r_{\text{up}})$ leads to the shift of the high-energy cutoff towards low energies, as expected. A considerable decrease in $v(r_{\text{up}})$ (up to $\sim c/3$) demands a decrease in γ for the existence of solutions in the framework of the model. Although such solutions contain a significantly cooler shock (up to $T_s \approx 9$ keV at $T_0 \approx 7$ keV for $\dot{M}_{17} = 3$), the relatively softer spectral tail remains nevertheless rather hard, and the PF distribution is similar to that given in Fig. 2. The possibility of the distinction of $v(r_{\text{up}})$ from the free-fall velocity was mentioned by Poutanen et al. (2013).

Within the models constructed under the grey approximation, the influence of the $m_e v^2/3$ term on the formation of the emergent spectrum (see an example in Fig. 8) manifests by adding a hard-energy tail to the typical quasi-Bose-Einstein distribution.

3.5 Free-free processes and the cyclotron emission

Free-free processes cause the increase in the brightness temperature of the emergent spectrum at the energies less ~ 0.5 keV in comparison to the case of pure scattering. It is shown clearly in the grey approximation (Fig. 8), in the framework of which the low energies are considered. The density of matter in the post-shock region is insufficient to make the free-free absorption an efficient mechanism of heating the plasma. Figs 7 and 9 represent the results of computations with free-free and cyclotron processes neglected. It is clear from these results that neglecting free-free pro-

cesses within the model does not vary the output distributions strongly and, thus, that the Compton energy exchange under the conditions of the local Compton equilibrium is the main mechanism of the heating of the plasma in the column (§ 3.3).

A more pronounced manifestation of free-free interactions could be obtained with the parameters differ from used here. This will be studied in the separate work. The $j_{\text{cyc}, i}$ terms cause only a small relative increase in the height of the mound (up to $\sim 5\%$) compared to the solution for the terms neglected. The combined action of free-free processes and the cyclotron emission leads to the model structures of a practically identical height for the cases considered (Figs 2 and 7), which is not the case in general (although there are no major differences expected).

Notice that the contribution of the overall seed radiation to the radiation energy density at the bottom is included in (27). Therefore, γ should insignificantly differ for the case of neglecting free-free processes inside the column (Fig. 7). The corresponding difference is small and neglected.

4 DISCUSSION

4.1 The model

The overall picture of matter breaking in the radiation-dominated regime is thus as follows. Five zones can be distinguished in the accretion channel above the magnetic pole: (1) the cold accretion flow falls near-freely in a radiation field of relatively low energy densities; (2) the flow begins to

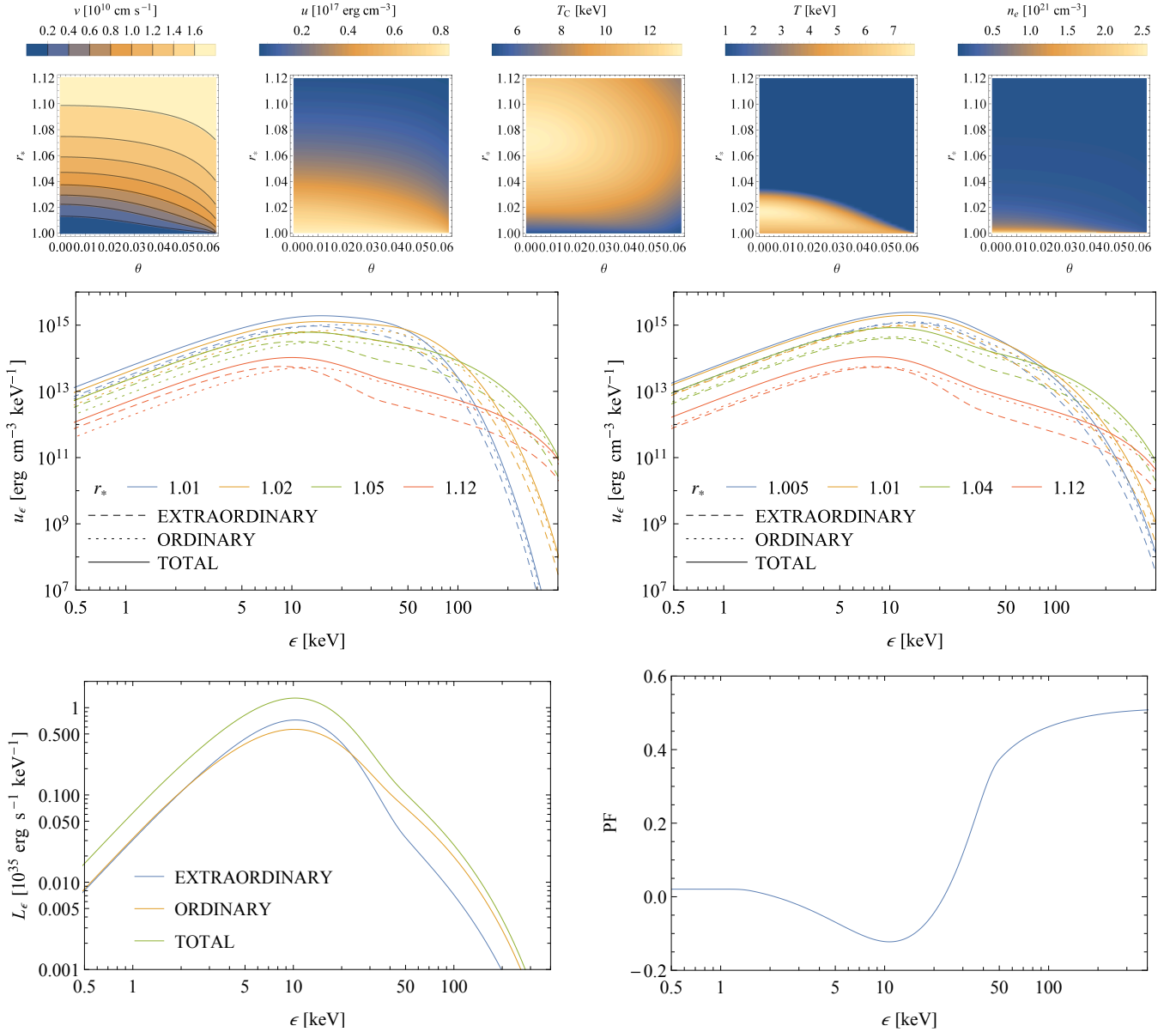


Figure 6. Same as Fig. 1, but for $\dot{M}_{17} = 0.2$. In the right panel, the spectral radiation energy density is shown for $\theta = 0.054$.

fluently brake in the shock, but its electron temperature is not yet very high; predominantly, the effect of second-order bulk Comptonization in this zone leads to the formation of the tails in the emergent continuum; (3) the flow experiences the rather sharp braking in high-density layers of the shock wave up to a near-complete stop, photons gain the energy in this zone due to first-order and second-order bulk Comptonization, and by thermal Comptonization; the plasma can be heated to 10–20 keV and higher by means of the bulk-heating mechanism there; (4) the matter falls, slowing down further, within a settling mound surrounded by the shock wave and the neutron star surface; as the matter settles, the electron temperature gradually approaches thermodynamically equilibrium one and becomes typically 1.5–4 times less than the temperature in the shock wave; (5) the plasma pen-

etrates through the magnetic field beyond the channel near the base of the emitting region.

The assumption of LTE is a typical example of that which cannot actually work in the shock wave. Thus, [Zhang et al. \(2021\)](#) have used the Stefan-Boltzmann law to write the radiation temperature for the balance equation, which caused the obtaining of too low electron temperature in the shock, where the Compton heating and cooling must be modelled, with the bulk-heating mechanism ([Blandford & Payne 1981b](#)) must be taken into account. The velocity profiles in the solutions without allowing for modelling thermal Comptonization are not very sensitive to the assumption on the electron temperature, since the radiative diffusive and enthalpy fluxes must not be strongly dependent on it ([Davidson 1973](#); [Arons et al. 1987](#)). Corresponding transfer equation for the total radiation energy density is obtained

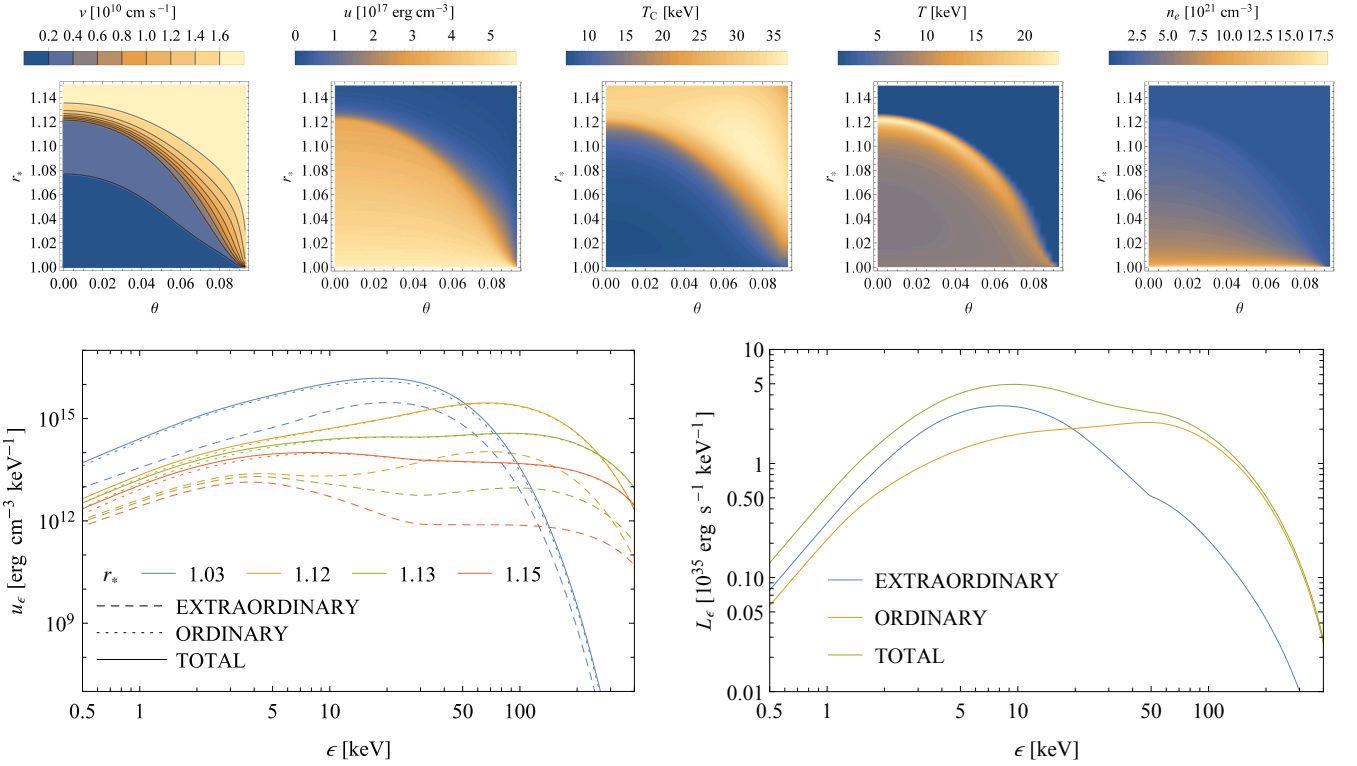


Figure 7. Same as Fig. 2, but free-free and cyclotron processes are neglected (panels for the local spectra at $\theta \neq 0$ and the polarization fraction are not shown).

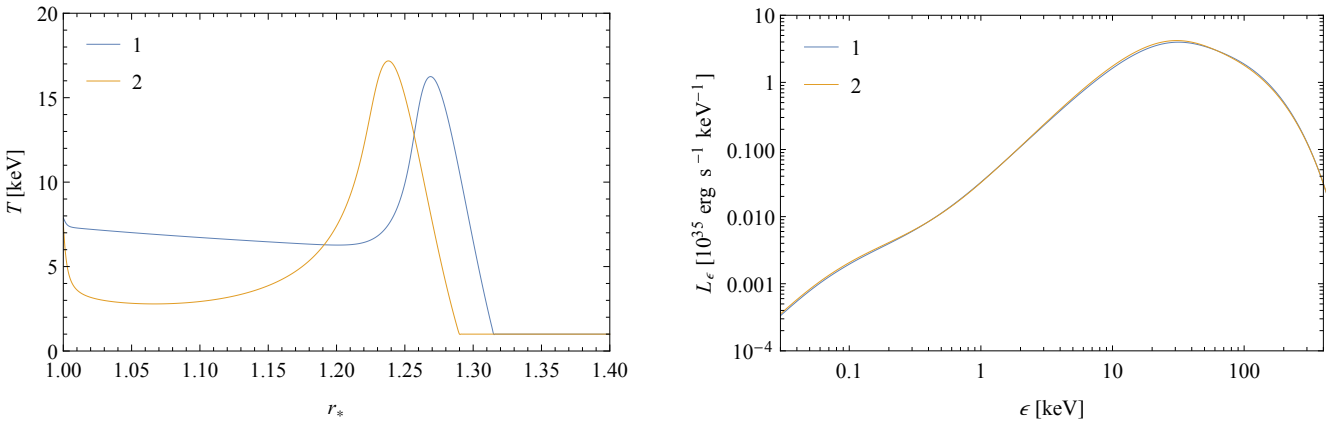


Figure 8. (Left) the electron temperature within the filled funnel plotted along the magnetic axis and (right) the emergent spectrum. The results obtained in the grey approximation for $\dot{M}_{17} = 3$: (1) all processes are included; (2) the induced Compton effect is ignored.

from the transfer equation for the spectral radiation energy density under the assumption about the Compton equilibrium (Appendix A).

The system of equations analysed by Zhang et al. (2021) (appendix A) corresponds to equations of G2021, but accounts for the effects of the gravitational acceleration and viscosity (the scattering is assumed to be isotropic). The viscosity terms are neglected during the consideration of the origination of photon bubbles in the WKB approximation. Since the development of photon bubble instability is related to perturbations of the mass density and total radiation flux,

its description should not be strongly dependent on the particular results for the electron temperature.

The process of the going out of the plasma beyond the column needs to be modelled in detail in the framework of MHD simulations. Simple estimates were made by Lyubarskii & Syunyaev (1988). One can obtain that the mass growing above the neutron star crust can originate between outpourings a dense gas-dominated non-steady thermalized layer of the height $Z \lesssim 2kTR^2/(GMm_p) \approx 60$ cm (for the constant temperature taken to be equal 6 keV). This layer, or ‘the thermal mound’ (Becker 1998), can be ignored

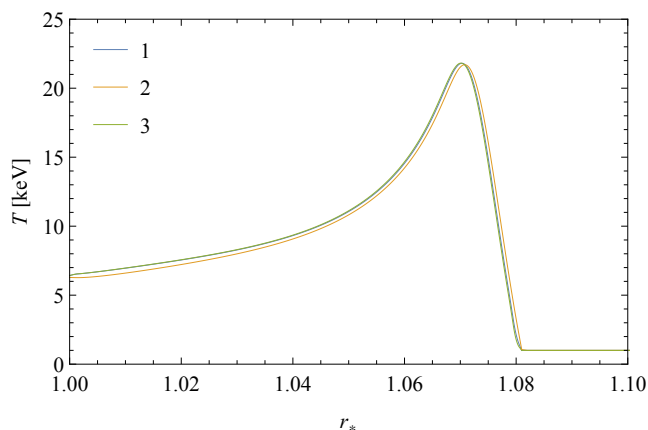


Figure 9. Electron temperature within the filled funnel plotted along the magnetic axis. The results of polarization- and spectrum-dependent calculations for $\dot{M}_{17} = 1$: (1) all processes are included (Fig. 1); (2) free-free processes, the cyclotron emission and the induced Compton effect are ignored; (3) free-free processes and the cyclotron emission are ignored.

in the calculations of the radiation transfer in the funnel, since its altitude is small and the energy exchange throughout the medium above the layer is significant.

The radiation energy density corresponding to the post-shock velocity equal to $1/7$ of the pre-shock value cannot serve for the implementation of the bottom boundary condition, since this post-shock value of the velocity was obtained for a typical infinite shock wave (e.g. [Zel'dovich & Raizer 1967](#)). The circumstances of X-ray pulsars (e.g. the boundedness of the settling mound by the neutron star surface, the transverse boundedness of the gas flow, the presence of a magnetic field) lead to $\gamma \sim 1$. The used value of γ leads to $v(R)$ of about $3 \times 10^8 - 4 \times 10^8$ cm s $^{-1}$. A reasonable variation in γ in both directions cannot change the results considerably (for $\gamma > 0.99$ a steady solution does not often exist yet).

The model described in Sections 2 and 3 does not imply the consideration and solution of the energy equation for the total radiation energy density (Appendix A). One can guess that its inclusion and thus the transition to solving two separate problems (obtaining the velocity profile, e.g. [Davidson \(1973\)](#), and then self-consistent calculation of the electron temperature and spectral radiation energy density) may appear more useful in some studies. Nevertheless, the method described in the present paper guarantees full compliance of all obtained distributions in the framework of hydrodynamical approach, providing better, as well as joint, fulfilment of the Liouville theorem. The self-consistent solutions take into account the result of calculating the realistic frequency photon redistribution, in contrast to the spectrum-integral approaches including the equations of a form of those of Appendix A.

As is clear from above, in the calculations aimed to obtain the dynamical structure and carried out with the use of the grey approximation it would be reasonable to use the scattering cross section along the field pretty close to the Planck and Rosseland means of the σ_1 quantity to achieve correct characteristic values of $\nabla \cdot \mathbf{v}$.

The Planck mean reads $\langle \sigma_1 \rangle_P = 40/21 (\pi kT/\epsilon_{cyc})^2 \sigma_T$ for $\epsilon_{cyc}/(kT)$ well exceeding $\pi\sqrt{2}$, and the Rosseland mean reads $\langle \sigma_1 \rangle_R = 4/5 (\pi kT/\epsilon_{cyc})^2 \sigma_T$ for $\epsilon_{cyc}/(kT)$ well exceeding π . The polarization-averaged Planck and Rosseland means calculated for the accurate magnetic opacities were presented by [Suleimanov et al. \(2022\)](#).

To obtain the results shown in Fig. 8, the less scattering cross section along the field compared with the specified means was used for computational reasons, which caused relatively more gentle profiles of the velocity within the shock. The use of small values $\sim 10^{-2} \sigma_T$ for that cross section would lead to a very smooth shock profile, so that the settling mound would be virtually absent. This means that there is no the same grey equivalent for obtaining simultaneously for the case of a strong magnetic field both the structure and the total spectrum, whose slope of the quasi-exponentially fallen power-law corresponds at characteristic values of the total y -parameter to a grey cross section along the field much smaller than $10^{-2} \sigma_T$.

The main drawback of the present work is the lack of calculations of the radiative transfer at frequencies of the cyclotron resonances, whose influence remains to be unstudied. In general, those calculations should be associated with the accurate scattering and absorption cross sections for a hot magnetized plasma calculated in the temperature range characteristic for the column (e.g. [Schwarm et al. 2017](#); [Suleimanov et al. 2022](#); [Mushtukov et al. 2022](#); [Mészáros 1992](#)). In principle, it is not difficult to incorporate into the codes the cross sections containing the cyclotron resonance (resonances) instead of the used cross sections, for which there is the only nuisance associated with the corresponding glaring retardation of the convergence. Another lack of the model developed is the description of the radiative transfer in the non-relativistic Fokker-Planck approximation. Comptonization is modelled using the angle-averaged cross sections, which is rather crude applied to the ordinary mode (variation of this quantity in the pretty wide range, however, does not affect the results dramatically). Solving a system of equations similar to that described in Section 2 and including the integro-differential transfer equations written for a moving medium of the funnel instead of expansions (5) would yield more accurate results containing angular distributions of the radiation intensity. Furthermore, the relativistic description of the radiative transfer should be used.

Although the photon energy dependence of the cross sections for both modes plays a crucial role in the spectrum formation, the role of terms containing the photon energy derivatives of the angle-averaged cross sections is insignificant. The mode switching is taken into account using the results of studies on the coupled-diffusion approximation of the radiative transfer ([Nagel 1981](#); [Kaminker, Pavlov & Shibano 1982](#); [Mészáros 1992](#)).

A few remarks should be made on the alternative calculations. A drawback of the existing 1D numerical and analytical models is that, in the framework of them, a significant part of the photons leave the column directly from the side-wall of the zone of the slowly falling gas, without crossing the shock wave, as was noted above. This process is often described by a term in the transfer equation written by means of the averaged diffusion time across the column ([Becker & Wolff 2007](#); [Farinelli et al. 2016](#); [West et al. 2017b](#)). A similar simple picture is typical for dynamical models of [Basko](#)

& Sunyaev (1976) and Tsygan (1977) constructed by means of averaging the radiation flux across the magnetic field. Calculations of the emergent spectrum with the use of 1D models may take into account the dynamical effects in the insufficient extent. Such models open a way to fit easily a vast amount of observations.

The solutions of Lyubarskii (1986) were obtained under the assumption of a phenomenological dependence of the photon occupation number on the optical depth. The shape of the obtained spectra at frequencies less than the frequency of maximum is artificial. The dynamical effects were not considered. These results led to the lack in important details in describing the formation of a continuum carried out by Postnov et al. (2015) (the radiation of the ordinary mode advected downwards in the shock wave was totally ignored).

4.2 On the fit of observations

The high-energy tails, expanding mainly due to the influence of second-order bulk Comptonization, can become an obstacle to fit observed fallen quasi-power-law spectra with the developed model. The received flux in the tails is often relatively low (e.g. Kühnel et al. 2017). If future simulations taken into account angular photon redistribution and cyclotron resonances do not lead to better agreement with observations at usual problem parameters, this will mean that either the velocity at the top boundary may be distinguished noticeably from the free-fall velocity (and then the simplest solution is in the parametrization of the velocity at the top) or the realistic profiles of the shock are much more complicated than obtained here and must be found in the spectral radiative transfer simulations coupled with the MHD simulations. An experimental explanation may consist in the absence of the corresponding observational data. The obtained hardness of the spectrum taken near the energies 10 keV and 1 keV may exceed the observational value because of ignoring the reproduction of the radiation in the atmosphere of a neutron star, the albedo of which is characterised by a low-frequency cutoff (Postnov et al. 2015).

Recently, the observed continuum of the radiation from the X-ray pulsar 1A 0535+262 generated during the giant outburst and having a high-energy spectral maximum at energies of $\sim 20\text{--}30$ keV has been described by Kong et al. (2022) and Shui et al. (2024). Another well-known source with similar spectral properties is V 0332+53 (Doroshenko et al. 2017). As an interpretation, one can consider the radiation with a spectral maximum in the vicinity of the maximum of the spectrum of the extraordinary mode from a strongly heated emitting region of a relatively small area (bulk Comptonization can contribute in the displacement of the maximum as described above). The approximate examples of the continuum of the corresponding form are shown in Fig. 4. The significant negative correlation of the CRSF energy with the X-ray luminosity within such a hot spectrum, being considered in the model directly relating the CRSF centroid energy to the height of the column, would imply a significant absolute difference in the height of the column in the considered states, which cannot be demonstrated by the narrow hollow column. (The relatively small height of the hollow columns was previously obtained in numerical simulations of Postnov et al. 2015.) The possible solution seems in taking into consideration the distortions in the magnetic

field strength occurring in the column (see examples of solutions of the Grad-Shafranov equation for preset mounds obtained by Mukherjee et al. 2013a and Mukherjee, Bhattacharya & Mignone 2013b). Weaker magnetic fields appearing with increasing \dot{M} would explain the observed anticorrelation of the CRSF energy with the X-ray luminosity. The check is to become the aim of further self-consistent MHD simulations.

Preliminary simulations in the current model with the surface value of the magnetic field strength less than considered above (it was set $\epsilon_{\text{cyc}}(R) = 10$ keV) lead to the two-hump total emergent spectrum with the location of the CRSF in the spectral saddle. The exact spectral shape is to be modelled in the framework of upcoming studies, which will also include the effects of complicated (non-dipole) geometry of a magnetic field.

Theoretical models of the column with a collisionless shock wave also lead to solutions corresponding very strong heating of the plasma (often up to tens of keV) during passing the shock wave (Langer & Rappaport 1982; Bykov & Krasil'shchikov 2004). In these models, the hot material fills the entire post-shock zone up to the neutron star atmosphere, which may be another problem for the interpretation of the observational data. In the calculations of Vybornov et al. (2017) using the Feautrier method, the electron temperature was parametrized to fit the observational spectra and appeared to be rather low (5–6 keV). Detailed self-consistent modelling of the spectrum of the radiation from the column with the collisionless shock is the problem that remains to be solved.

The formation at temperatures $\sim T_{\text{eff}} - T_0$ and under circumstances not considered here of the spectra having the maximum in corresponding to these temperatures spectral range and a high-energy power-law should be studied further.

5 CONCLUSIONS

The accretion regime on to a strongly magnetized neutron star corresponding to luminosities above the value of L_{cr} has been considered. The main processes within the magnetic polar funnels have been investigated. The transfer equations for the polarized radiation have been numerically solved within the considered domains self-consistently with the expressions for the electron temperature and the radiation energy density, the momentum equation, and the continuity equation. The solutions obtained describe the dynamical and thermal structure both of the radiation-dominated shock wave and the settling mound, and the polarimetric X-ray continuum of radiation that emerges from the funnel.

It has been found that the peak height of the model accretion column, being calculated taking into account the specific form of the frequency- and polarization-dependent scattering cross sections, can depend nonlinearly on the accretion rate, in contrast to the nearly linear outputs obtained in the grey approximation. In the case of a sufficiently strong magnetic field, the saturation in the column peak height–accretion rate dependence takes place in the studied range of the accretion rate.

The significance of the Compton scatterings within the accretion column is as great as it is characteristic, for exam-

ple, for the early universe. Comptonization has been shown to be the main process for the formation of the temperature structure of the column. The electrons are in the thermodynamic equilibrium with the radiation deep below the shock wave, as proofed in the way of using the Compton-equilibrium formula for obtaining the electron temperature, which noticeably exceeds the blackbody value within the shock due to the contribution of the effects of bulk motion to the heating of the plasma.

The temperature structure should be calculated in general case with taking into account the influence of the induced Compton effect, which impact on the electron temperature within the settling mound under the condition of the sufficiently weak magnetic field and (at the sufficient accretion rate) on the existence of the steady-state solutions of the problem. The effects of second-order bulk Comptonization are important mainly for the formation of the spectra of emergent radiation, resulting in a smoothed power-law high-energy zone with a cutoff. I have discussed main directions for updating the results in the framework of more accurate models.

The calculated absolute value of the polarization fraction lies between 0.05 and 0.5 being measured near the spectral maximum of the extraordinary mode. The model developed can provide the emergent continuum of the ordinary mode close to that of the extraordinary mode. Namely, the calculations for the configuration of a geometrically thin hollow column can lead to the spectrum of the funnel characterised by a high-energy maximum and a low polarization fraction over the entire spectral range. The similar picture for the cooler spectra is typical for the filled radiation-dominated column at sufficiently low accretion rates below $\dot{M}_{17} = 1$ that are close to the critical value.

ACKNOWLEDGEMENTS

I thank R. Staubert and R. Rothschild for their responses. The work was supported by the Foundation for the Advancement of Theoretical Physics and Mathematics ‘BASIS’ (grant 17-15-506-1).

DATA AVAILABILITY

The calculations described in this paper were performed using the private codes developed by the author. The data presented in the figures are available on reasonable request.

REFERENCES

- Adler S. L., Bahcall J. N., Callan C. G., Rosenbluth M. N., 1970, *PhRvL*, **25**, 1061
- Alexander S. G., Meszaros P., Bussard R. W., 1989, *ApJ*, **342**, 928
- Arons J., 1992, *ApJ*, **388**, 561
- Arons J., Klein R. I., Lea S. M., 1987, *ApJ*, **312**, 666
- Baan W. A., Treves A., 1973, *A&A*, **22**, 421
- Basko M. M., Sunyaev R. A., 1976, *MNRAS*, **175**, 395
- Becker P. A., 1998, *ApJ*, **498**, 790
- Becker P. A., Wolff M. T., 2005, *ApJ*, **630**, 465
- Becker P. A., Wolff M. T., 2007, *ApJ*, **654**, 435
- Becker P. A., Wolff M. T., 2022, *ApJ*, **939**, 67
- Bisnovatyi-Kogan G. S., Fridman A. M., 1970, *SvA*, **13**, 566
- Blandford R. D., Payne D. G., 1981a, *MNRAS*, **194**, 1033
- Blandford R. D., Payne D. G., 1981b, *MNRAS*, **194**, 1041
- Burnard D. J., Klein R. I., Arons J., 1988, *ApJ*, **324**, 1001
- Burnard D. J., Klein R. I., Arons J., 1990, *ApJ*, **349**, 262
- Burnard D. J., Arons J., Klein R. I., 1991, *ApJ*, **367**, 575
- Bykov A. M., Krasil’shchikov A. M., 2004, *AstL*, **30**, 309
- Canuto V., Lodenquai J., Ruderman M., 1971, *PhRvD*, **3**, 2303
- Chandrasekhar S., 1960, Radiative transfer. Dover Publications, Inc., New York
- Davidson K., 1973, *NPhS*, **246**, 1
- Davidson K., Ostriker J. P., 1973, *ApJ*, **179**, 585
- Doroshenko V., Tsygankov S. S., Mushtukov A. A., Lutovinov A. A., Santangelo A., Suleimanov V. F., Poutanen J., 2017, *MNRAS*, **466**, 2143
- Farinelli R., Ceccobello C., Romano P., Titarchuk L., 2012, *A&A*, **538**, A67
- Farinelli R., Ferrigno C., Bozzo E., Becker P. A., 2016, *A&A*, **591**, A29
- Giacconi R., Gursky H., Kellogg E., Schreier E., Tananbaum H., 1971, *ApJL*, **167**, L67
- Ginzburg V. L., 1970, The propagation of electromagnetic waves in plasmas. Pergamon Press, Oxford
- Gnedin Y. N., Pavlov G. G., 1974, *JETP*, **38**, 903
- Gornostaev M. I., 2019, Postgraduate qualifying research paper, MSU, Moscow
- Gornostaev M. I., 2021, *MNRAS*, **501**, 564
- Hsu J. J. L., Arons J., Klein R. I., 1997, *ApJ*, **478**, 663
- Illarionov A. F., Syunyaev R. A., 1975a, *SvA*, **18**, 413
- Illarionov A. F., Syunyaev R. A., 1975b, *SvA*, **18**, 691
- Kalitkin N. N., 1978, Numerical methods. Nauka, Moscow
- Kaminker A. D., Pavlov G. G., Shibanov I. A., 1982, *Ap&SS*, **86**, 249
- Karzas W. J., Latter R., 1961, *ApJS*, **6**, 167
- Kirk J. G., 1985, *A&A*, **142**, 430
- Klein R. I., Arons J., 1989, in Hunt J., Battrick B., eds, ESA Special Publication Vol. 1, Two Topics in X-Ray Astronomy, Volume 1: X Ray Binaries. Volume 2: AGN and the X Ray Background. p. 89
- Klein R. I., Arons J., Jernigan G., Hsu J. J. L., 1996, *ApJL*, **457**, 85
- Klochkov D., Staubert R., Santangelo A., Rothschild R. E., Ferrigno C., 2011, *A&A*, **532**, A126
- Kompaneets A. S., 1956, *ZhETF*, **31**, 876
- Kong L.-D., et al., 2022, *ApJ*, **932**, 106
- Kraus U., Herold H., Maile T., Nollert H. P., Rebetzky A., 1989, *A&A*, **223**, 246
- Kühnel M., et al., 2017, *A&A*, **607**, A88
- Lamb F. K., Pethick C. J., Pines D., 1973, *ApJ*, **184**, 271
- Langer S. H., Rappaport S., 1982, *ApJ*, **257**, 733
- Levich E. V., Sunyaev R. A., 1970, *ApL*, **7**, 69
- Lodenquai J., Canuto V., Ruderman M., Tsuruta S., 1974, *ApJ*, **190**, 141
- Long X., et al., 2023, *ApJ*, **950**, 76
- Lyubarskii Y. É., 1986, *Ap*, **25**, 577
- Lyubarskii Y. E., Syunyaev R. A., 1982, *SvAL*, **8**, 330
- Lyubarskii Y. E., Syunyaev R. A., 1988, *SvAL*, **14**, 390
- Lyutikov M., Gavriil F. P., 2006, *MNRAS*, **368**, 690
- Maile T., Bock U., Herold H., Rebetzky A., Ruder H., 1989, *A&A*, **223**, 251
- Makishima K., et al., 1990, *ApJL*, **365**, L59
- Marshak R. E., 1958, *PhFl*, **1**, 24
- Mészáros P., 1992, High-energy radiation from magnetized neutron stars. University of Chicago Press, Chicago, IL
- Meszaros P., Pavlov G. G., Shibanov I. A., 1989, *ApJ*, **337**, 426
- Mihalas D., 1978, Stellar atmospheres. W. H. Freeman & Co., San Francisco

Mukherjee D., Bhattacharya D., Mignone A., 2013a, *MNRAS*, **430**, 1976
 Mukherjee D., Bhattacharya D., Mignone A., 2013b, *MNRAS*, **435**, 718
 Mushtukov A. A., Suleimanov V. F., Tsygankov S. S., Poutanen J., 2015a, *MNRAS*, **447**, 1847
 Mushtukov A. A., Tsygankov S. S., Serber A. V., Suleimanov V. F., Poutanen J., 2015b, *MNRAS*, **454**, 2714
 Mushtukov A. A., Markozov I. D., Suleimanov V. F., Nagirner D. I., Kaminker A. D., Potekhin A. Y., Portegies Zwart S., 2022, *PhRvD*, **105**, 103027
 Nagel W., 1981, *ApJ*, **251**, 278
 Postnov K. A., Gornostaev M. I., Klochkov D., Laplace E., Lukin V. V., Shakura N. I., 2015, *MNRAS*, **452**, 1601
 Poutanen J., Mushtukov A. A., Suleimanov V. F., Tsygankov S. S., Nagirner D. I., Doroshenko V., Lutovinov A. A., 2013, *ApJ*, **777**, 115
 Press W. H., Flannery B. P., Vetterling W. T., Teukolsky S. A., 1992, *Numerical Recipes in C. The Art of Scientific Computing*. Cambridge University Press, Cambridge
 Pringle J. E., Rees M. J., 1972, *A&A*, **21**, 1
 Psaltis D., Lamb F. K., 1997, *ApJ*, **488**, 881
 Psaltis D., Lamb F. K., 1999, in Poutanen J., Svensson R., eds, *Astronomical Society of the Pacific Conference Series Vol. 161, High Energy Processes in Accreting Black Holes*. p. 410
 Rebetzky A., Herold H., Maile T., Ruder H., Wolf K., 1988, *A&A*, **205**, 215
 Rebetzky A., Bock U., Herold H., Kraus U., Maile T., 1989, *A&A*, **225**, 137
 Riffert H., 1988, *ApJ*, **327**, 760
 Rothschild R. E., et al., 2017, *MNRAS*, **466**, 2752
 Rybicki G. B., Lightman A. P., 1979, *Radiative processes in astrophysics*. Wiley & Sons, New York
 Samarskii A. A., 1962, *ZVMMF*, **2**, 25
 Samarskii A. A., 2001, *The theory of difference schemes*. Marcel Dekker, inc., New York, Base
 Schwarm F. W., et al., 2017, *A&A*, **597**, A3
 Shapiro S. L., Salpeter E. E., 1975, *ApJ*, **198**, 671
 Shapiro S. L., Teukolsky S. A., 1983, *Black holes, white dwarfs and neutron stars: the physics of compact objects*. Wiley & Sons, New York
 Shui Q. C., et al., 2024, *MNRAS*, **528**, 7320
 Staubert R., Shakura N. I., Postnov K., Wilms J., Rothschild R. E., Coburn W., Rodina L., Klochkov D., 2007, *A&A*, **465**, L25
 Staubert R., et al., 2019, *A&A*, **622**, A61
 Suleimanov V. F., Mushtukov A. A., Ognev I., Doroshenko V. A., Werner K., 2022, *MNRAS*, **517**, 4022
 Titarchuk L., Mastichiadis A., Kylafis N. D., 1997, *ApJ*, **487**, 834
 Truemper J., Pietsch W., Reppin C., Voges W., Staubert R., Kendziorra E., 1978, *ApJL*, **219**, 105
 Tsygan A. I., 1977, *A&A*, **60**, 39
 Tsygankov S. S., Lutovinov A. A., Churazov E. M., Sunyaev R. A., 2006, *MNRAS*, **371**, 19
 Tsygankov S. S., et al., 2022, *ApJL*, **941**, L14
 Ventura J., Nagel W., Meszaros P., 1979, *ApJL*, **233**, 125
 Vybornov V., Klochkov D., Gornostaev M., Postnov K., Sokolova-Lapa E., Staubert R., Pottschmidt K., Santangelo A., 2017, *A&A*, **601**, A126
 Vybornov V., Doroshenko V., Staubert R., Santangelo A., 2018, *A&A*, **610**, A88
 Wang Y. M., Frank J., 1981, *A&A*, **93**, 255
 West B. F., Wolfram K. D., Becker P. A., 2017a, *ApJ*, **835**, 129
 West B. F., Wolfram K. D., Becker P. A., 2017b, *ApJ*, **835**, 130
 Zel'dovich Y. B., Illarionov A. F., 1974, *JETP*, **38**, 643
 Zel'dovich Y. B., Levich E. V., 1970, *JETPL*, **11**, 35
 Zel'dovich Y. B., Raizer Y. P., 1967, *Physics of shock waves and high-temperature hydrodynamic phenomena*. Academic Press, New York

Press, New York
 Zhang L., Blaes O., Jiang Y.-F., 2021, *MNRAS*, **508**, 617
 Zhang L., Blaes O., Jiang Y.-F., 2022, *MNRAS*, **515**, 4371
 de Hoffmann F., Teller E., 1950, *PhRv*, **80**, 692

APPENDIX A: EQUATIONS FOR THE TOTAL RADIATION ENERGY DENSITY

The physical model considered above does not contain any of transfer equations for the total radiation energy density. Nevertheless, let us consider them, limiting to consideration regardless of the polarization of radiation.

Let free-free and cyclotron processes be neglected and the term of the second order in the bulk velocity be ignored. Then it follows from the transfer equation (Blandford & Payne 1981a) that in a steady situation (the subscript ‘np’ for the occupation number and radiation energy density will be dropped)

$$\begin{aligned}
 & \nabla \cdot (\hat{D}\nabla u) - \mathbf{v} \cdot \nabla u - \frac{4}{3}u\nabla \cdot \mathbf{v} \\
 & + \frac{\sigma n_e}{m_e c} u \left(4kT - \bar{\epsilon} - \frac{\int_0^\infty \epsilon^4 n^2 d\epsilon}{\int_0^\infty \epsilon^3 n d\epsilon} \right) = 0,
 \end{aligned} \tag{A1}$$

where \hat{D} is the diffusion tensor, the cross section σ is represented analogously to expression (25) of Blandford & Payne (1981a) with accuracy to accounting for the n^2 term, and

$$\bar{\epsilon} = \frac{\int_0^\infty \epsilon^4 n d\epsilon}{\int_0^\infty \epsilon^3 n d\epsilon}. \tag{A2}$$

Using (19) one can obtain from (A1)

$$\nabla \cdot \mathbf{F} = \frac{1}{3}\mathbf{v} \cdot \nabla u, \tag{A3}$$

where

$$\mathbf{F} = -\hat{D}\nabla u + \frac{4}{3}u\mathbf{v} \tag{A4}$$

is the total radiation flux. If the momentum equation is considered in the form (2), then from (2) and (A3) one can obtain (Davidson 1973)

$$\nabla \cdot \mathbf{F} = -\frac{1}{2}n_e m_p \mathbf{v} \cdot \nabla v^2. \tag{A5}$$

If the gravitational acceleration is not neglected, the momentum equation reads (Wang & Frank 1981)

$$n_e m_p (\mathbf{v}\nabla)\mathbf{v} = -\frac{\nabla u}{3} - \frac{GMn_e m_p}{r^2} \frac{\mathbf{r}}{r}, \tag{A6}$$

where \mathbf{r} is the vector directed from the neutron star, the length of which is counted as r ; the difference from the usual distance to the neutron star centre is neglected in the last term for the values of r under consideration (because of the direction of the velocity, where appropriate, one could limit oneself to using the derivatives with respect to r and the v quantity). Collecting (A3) and (A6) yields (Wang & Frank 1981)

$$\nabla \cdot \mathbf{F} = -n_e m_p \mathbf{v} \cdot \nabla \left(\frac{v^2}{2} - \frac{GM}{r} \right), \tag{A7}$$

which can easily be written out straightforwardly from the energy conservation law, as well as (A5).

These equations are crudely valid while the flow is not too dense, and hence free-free processes are not important. Let the second-order bulk Comptonization term be now taken into account. Without specification of the terms taken into account in the right-hand side of the momentum equation and of the way of the calculation of T , one has for the non-steady case (e.g. West et al. 2017b)

$$\nabla \cdot \mathbf{F} + \frac{\partial u}{\partial t} = \frac{1}{3} \mathbf{v} \cdot \nabla u + \frac{4\sigma n_e u}{m_e c} \left(k(T - T_{C, np}) + \frac{m_e v^2}{3} \right) + S, \quad (\text{A8})$$

where t is time and S may include the terms responding for free-free and cyclotron processes.